Atypical Josephson effect in hybrid superconductor-hole systems

Peter D. Johannsen,[1,*] Henry F. Legg,[1,2] Stefano Bosco,[1,3] Daniel Loss,[1] and Jelena Klinovaja[1]
[1]*Department of Physics, University of Basel, Klingelbergstrasse 82, 4056 Basel, Switzerland*
[2]*SUPA, School of Physics and Astronomy, University of St Andrews, North Haugh, St Andrews KY16 9SS, United Kingdom*
[3]*QuTech, Delft University of Technology, Delft, The Netherlands*

(Received 6 May 2025; accepted 28 January 2026; published 17 March 2026)

We consider hybrid systems consisting of a hole-doped semiconductor coupled to electronic states of finite-size superconductors, where the opposite sign of the masses in the two subsystems gives rise to insulating gaps at subband anticrossings. Consequently, increasing the coupling strength to the superconductor can paradoxically suppress the proximity-induced superconductivity in the semiconductor by enhancing these insulating gaps. We demonstrate that the presence of such induced insulating gaps leads to a characteristic atypical behavior of the critical supercurrent in Josephson junctions based on these hybrid structures. Our findings provide important insights for the design of robust quantum computing platforms utilizing hybrid superconductor-hole systems.

DOI: 10.1103/dqgc-8crs

I. INTRODUCTION

Over the past decade, the usage of hole gases in semiconductor devices—such as germanium (Ge)—has surged, in part due to the prospective scalability of these devices for future quantum computing purposes and in part because of the recent technological improvements in fabrication [1–3]. Furthermore, hole gases present strong, tunable spin-orbit interactions, allowing for electrostatic control of system properties [1,4–18] and tunable coupling to nuclear spins [19–21]. Many potential quantum computing platforms utilize hole gases [22–29]. However, hybrid superconductor-semiconductor devices, in which thin superconducting (SC) layers are brought into contact with a semiconductor such as a two-dimensional hole (electron) gas [2DHG (2DEG)] [30–33], not only host Andreev bound states—the building block of Andreev spin qubits [34–37]—but they have also recently been proposed as platforms for topological superconductivity [38–43].

Central to hybrid superconductor-semiconductor systems is the superconducting proximity effect, in which a parent superconductor induces an SC pairing in a semiconductor. The proximity effect in electron systems has been the subject of extensive study, both experimentally and theoretically [44–51]. While the proximity effect in hole gases exhibits many similarities to its electron counterpart, there is also a unique phenomenology and this can result in non-trivial effects [30–33,52–66]. For instance, surprisingly, it was recently observed that a strong coupling between a hole gas in Ge and a superconductor can reduce the proximity effect [31,32], which would lead to undesirable device characteristics for quantum computing applications. In hybrid devices, the regime of most interest is when the proximity-induced pairing is of the same order of magnitude as in the parent superconductor. If the crossing between a subband of a 2DEG and a metallic sub-

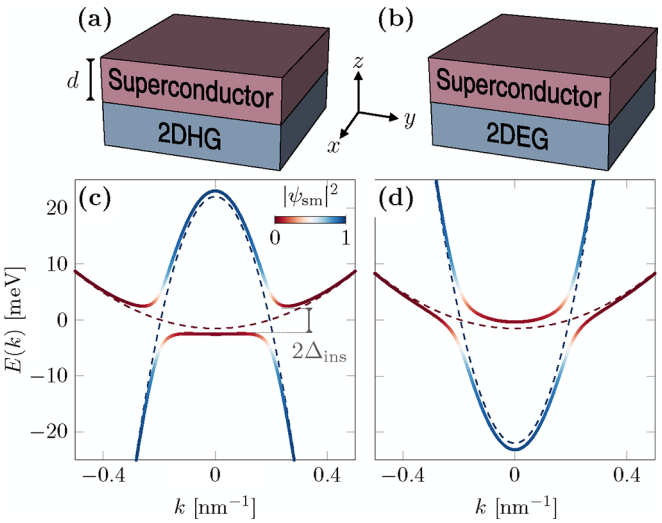

FIG. 1. A hybrid superconductor-semiconductor system with an SC layer of thickness d on top of a semiconductor [(a) 2DHG and (b) 2DEG]. The tunnel coupling t between a semiconductor and the SC subband with smallest momentum can result in an insulating gap, $2\Delta_{ins}$ [indicated by the gray bar in panel (c)], or an avoided crossing [as is shown in panel (d)], depending on the sign of the mass. The hybridization between the subbands can be characterized by the weight in the semiconductor, $|\psi_{sm}|^2$, which is indicated by the color of the dispersions in panels (c) and (d) [see colorbar in panel (c) and Appendix A]. Here, $m_{sc} = 0.95m_e$ and $m_{sm} = \pm 0.07m_e$, where m_{sc} and m_{sm} refer to the effective masses in the superconductor and semiconductor, respectively [39,40,67], with m_e the bare electron mass. The parameters used are $t = 5$ meV, $\mu_{sm} = 22$ meV, and $\Delta_0 = 0$, and the effective SC subband chemical potential is $\bar{\mu}_{sc} = 1.5$ meV.

*Contact author: peterdaniel.johannsen@unibas.ch

band in the superconductor is close to the chemical potential μ of the coupled system, the proximity effect is most pronounced [see Fig. 1(d)]. In this case, the strong hybridization between the two subsystems results in a substantial SC gap in the semiconducting subsystem [44–46]. In contrast, due to the opposite signs of the effective masses, coupling a 2DHG subband to a metallic subband results in an *insulating* gap in the energy spectrum [see Fig. 1(c)], such that there are no states with a significant weight in the semiconductor in this energy range. The absence of states at the chemical potential in the 2DHG suggests that the SC proximity effect will be suppressed close to such subband crossings. As a result, in such a setup, we expect an interesting interplay between these insulating and SC gaps.

Interestingly, we find that the presence of insulating gaps can imply that *increasing* the coupling between the subsystems can result in a *reduction* of the proximity-induced SC pairing in the semiconductor. We demonstrate how this effect can be observed in one-dimensional (1D) Josephson junctions (JJs). Our results are most relevant to systems in which SC subbands are well-defined, i.e. the mean-free path in the superconductor is longer than the layer thickness, which in turn is assumed to be much shorter than the SC coherence length. This is a regime only recently accessible experimentally and could explain the inconsistent SC proximity effect recently observed in hybrid Ge devices [31,32]. Our main results are valid both for one- and two-dimensional coupled systems [44–46], whereas the JJ analysis is done for nanowire systems.

II. MODEL

To model the proximity effect in hybrid superconductor-semiconductor devices, we consider a thin 2DHG (2DEG) coupled to an SC layer of thickness d (along z direction, see Fig. 1). The superconductor is assumed to have a parabolic dispersion with positive mass $m_{\rm sc}$, an s-wave pairing amplitude Δ_0, and to be described by the Bogoliubov-de Gennes (BdG) Hamiltonian

$$H_{{\rm sc},k} = \left(\frac{k^2 - \partial_z^2}{2m_{\rm sc}} - \mu_{\rm sc}\right)\eta_z + \Delta_0\eta_x, \tag{1}$$

where η_i denotes the ith Pauli matrix in Nambu space, $\mu_{\rm sc}$ is the chemical potential in the superconductor, and $k = (k_x^2 + k_y^2)^{1/2}$ is the in-plane momentum ($\hbar = 1$). The finite thickness of the superconductor defines multiple subbands, of which $2\lfloor k_F d/\pi \rfloor$ are occupied (factor of two due to spin degeneracy). The semiconducting layer consists of a single spin-degenerate parabolic subband with a negative (positive) effective mass $m_{\rm sm}$, describing a 2DHG (2DEG) subband, such that the Hamiltonian is given by

$$H_{{\rm sm},k} = \left(\frac{k^2}{2m_{\rm sm}} - {\rm sgn}(m_{\rm sm})\mu_{\rm sm}\right)\eta_z, \tag{2}$$

where $\mu_{\rm sm}$ is the chemical potential in the semiconductor. We use ${\rm sgn}(m_{\rm sm})\mu_{\rm sm}$ to ensure that $\mu_{\rm sm} > 0$ gives rise to occupied states in the semiconductor. We note that, due to the rotational invariance of the Hamiltonians defined in Eqs. (1) and (2), the energy spectra depend only on k. Thus, the results in this work also pertain to 1D systems (see Refs. [44,45]).

We are interested in the low-energy physics in the subband of the semiconductor, which, especially in the presence of strain and in the absence of inversion-symmetry breaking, implies that it is appropriate to use the effective mass approximation [7]. We note that the full Luttinger-Kohn description does not modify the results in this work. The coupling between the superconductor and semiconductor is assumed to be independent of momentum and to occur at the interface $z = z_0$ [45] (see Appendix A).

In this work, we focus on the parameter regime where there is only a single SC subband that is strongly tunnel coupled to the semiconductor subband (with amplitude t). Therefore, there is only a single metallic subband that is strongly coupled to the semiconducting subband [see Figs. 2(a) and 2(b)]. All other subbands are gapped by $\approx \Delta_0$ [see Fig. 2(c)] and are therefore assumed not to contribute to the phenomena of interest in this work. The subband spacing in the superconductor due to the hard-wall confinement, $\delta E_{\rm sc} = \pi v_F/d \approx 75\,{\rm meV}$, and $\mu_{\rm sc}$ are assumed to be the largest energies in the system (v_F is the Fermi velocity in the superconductor).

Proximity effect. The proximity effect can be taken into account using the self-energy, $\Sigma_{k,\omega}$, obtained by solving the Dyson equation for the full Matsubara Green's function of the semiconductor

$$G_{k,\omega} = (i\omega - H_{{\rm sm},k} - \Sigma_{k,\omega})^{-1}, \tag{3}$$

where ω is a Matsubara frequency. In particular, the self-energy can be written as [44,45]

$$\Sigma_{k,\omega} = (i\omega - \Delta_0\eta_x)\left(1 - \Gamma_{k,\omega}^{-1}\right) - \delta\mu_{k,\omega}\eta_z. \tag{4}$$

The functions $(1 - \Gamma_{k,\omega}^{-1})$ and $\delta\mu_{k,\omega}$ have simple poles at the energy levels of the SC. As described in Ref. [45], they can be expressed as

$$\begin{aligned}
\Gamma_{k,\omega} = \Bigg(1 + \frac{\gamma}{\Omega\varphi[\cosh(2\chi d) - \cos(2\zeta d)]} \\
\times \{\sinh(2\chi d) - \cos(2\zeta z_0)\sinh[2\chi(d - z_0)] \\
- \cos[2\zeta(d - z_0)]\sinh(2\chi z_0)\}\Bigg)^{-1}, \\
\delta\mu_{k,\omega} = -\frac{\gamma}{\varphi[\cosh(2\chi d) - \cos(2\zeta d)]} \\
\times \{\sinh(2\zeta d) - \sin(2\zeta z_0)\cosh[2\chi(d - z_0)] \\
- \sin[2\zeta(d - z_0)]\cosh(2\chi z_0)\},
\end{aligned} \tag{5}$$

where we define

$$\begin{aligned}
&\varphi = \sqrt{1 - k^2/k_F^2}, \quad \zeta = k_F\varphi, \\
&\Omega = \sqrt{\Delta_0^2 + \omega^2}, \quad \chi = 2m_{\rm sc}\Omega/\zeta, \quad \gamma = t_0^2/v_F,
\end{aligned} \tag{6}$$

where t_0 is the hopping amplitude between the subsystems. The lower boundary of the SC layer is located at $z = 0$, while the 2DH(E)G is located at $z = z_0$ for $0 \leqslant z_0 \leqslant d$.

A. Renormalized dispersions

After analytic continuation, we numerically determine the poles of the full retarded Green's function $G^R_{k,\omega}$, which define

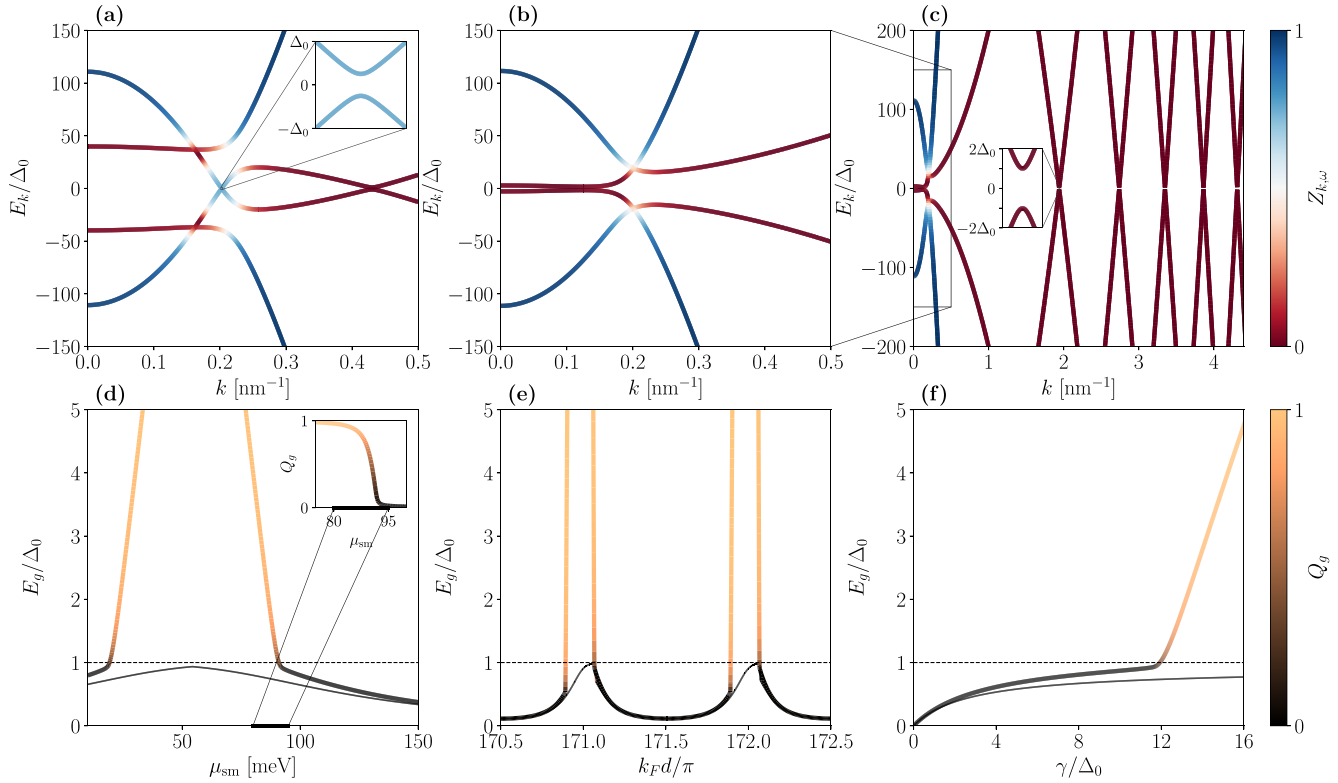

FIG. 2. The induced gap E_g in the spectrum $E(k)$ of a hybrid superconductor-2DHG can be (a) smaller or (b) larger than Δ_0 of the superconductor. While for proximity-induced pairing gap $E_g \leqslant \Delta_0$ [see the inset in panel (a)] in the SC phase, we find $E_g > \Delta_0$ in the insulating phase (b). The insulating phase emerges when the 2DHG and SC subbands cross close to μ [see also Fig. 1(c)]. However, the other SC subbands at larger momenta remain gapped only by Δ_0 [see inset in panel (c)]. The relative position of the subbands can be tuned by adjusting (d) μ_{sm} or (e) $k_F d$. For 2DEGs [thin lines in panels (d) and (e)], $E_g \leqslant \Delta_0$ corresponds to the SC proximity gap. In contrast, 2DHGs are in the insulating phase at the same parameter values at which the SC pairing is at its maximum in the 2DEG. When $E_g > \Delta_0$, the BCS charge, Q_g, approaches unity, implying a suppression of the proximity pairing. In contrast, $Q_g \approx 0$ when $E_g \leqslant \Delta_0$, implying an almost equal linear combination of quasiparticles and quasiholes, and thus Q_g offers a convenient indicator of the loss of superconducting correlations. (f) As expected for a 2DEG (thin line), $E_g \to \Delta_0$ as $\gamma \gg \Delta_0$. In contrast, for a 2DHG (thick line) $E_g \gg \Delta_0$ for large γ with $Q_g \to 1$, i.e., increasing γ strongly *reduces* the SC proximity effect. (a)–(c) $\gamma = \Delta_0$, (d) $\gamma = 2\Delta_0$, and (e) $\gamma = 25\Delta_0$, where $\Delta_0 = 0.2$ meV, while $k_F d/\pi = 172.05, 172, 172, 172.025, 171.05$ in panels (a)–(d) and (f), respectively. We set $d = 30$ nm and vary k_F, additionally, $\mu_{sm} = 22$ meV in panels (a)–(c), (e) and (f), and $\mu_{sc} = 13$ eV everywhere. Finally, $z_0 = \lambda_F/7$, where $\lambda_F \approx 0.35$ nm is the Fermi wavelength in the superconductor. The effective masses are as in Fig. 1.

the renormalized dispersion relation $E(k)$ in the semiconductor. The renormalized energy spectrum is shown in Fig. 2, comparing [Fig. 2(a)] the insulating and [Figs. 2(b) and 2(c)] the proximitized SC phases, where in panel (c) we show a few additional SC subbands at larger momenta. We define the gap in the energy spectrum as $E_g = \min_{k<k_c} |E(k)|$, where the cutoff k_c is chosen to capture the minimum of the semiconductor band at the smallest momentum. Additionally, we define k_g as the momentum where $E(k_g) = E_g$ and $(H_{sm,k_g} + \Sigma_{k_g,E_g})|k_g, E_g\rangle = E_g|k_g, E_g\rangle$. Importantly, E_g corresponds to the excitation gap in the semiconductor, which does not necessarily match the proximity-induced SC pairing gap. Remarkably, E_g can exceed Δ_0 if the system is in the insulating phase, where an intrinsic insulating gap $2\Delta_{ins}$ with

$$\Delta_{ins} = \frac{2t\sqrt{m_{sc}|m_{sm}|}}{m_{sc} + |m_{sm}|} = \frac{2t\sqrt{v_{sc}|v_{sm}|}}{v_{sc} + |v_{sm}|} \tag{7}$$

exists even when $\Delta_0 = 0$ [see Fig. 1(c)]. Here, v_{sc} (v_{sm}) is the Fermi velocity of the relevant superconducting (semiconducting) subbands. We refer to Appendix B for an effective two-band model description of the insulating gaps.

To obtain $E_g > \Delta_0$ is indeed possible if the chemical potential is close to the anticrossing between the 2DHG subband and one of the metallic subbands of the superconductor. Moreover, E_g for 2DHGs can exceed the corresponding value for 2DEGs even when $E_g < \Delta_0$ [see Figs. 2(d)–2(f)], without significantly suppressing SC properties. This suggests that the insulating gap can enhance the proximity gap while maintaining robust pairing.

In this work, we define the insulating phase as $E_g > \Delta_0$; however, it should be noted that the transition between SC and insulating phases is gradual, especially on the scale of the temperature of SC systems, and on the scale of Δ_0, as can be seen in the insert of Fig. 2(d). However, for the purpose of this work, we will treat the phases as distinct.

As shown in Figs. 2(d)–2(f), insulating phases and SC phases with strong proximity-induced SC pairing are close to each other. As such, extra care is required to differentiate between a semiconductor with a large pairing gap and one

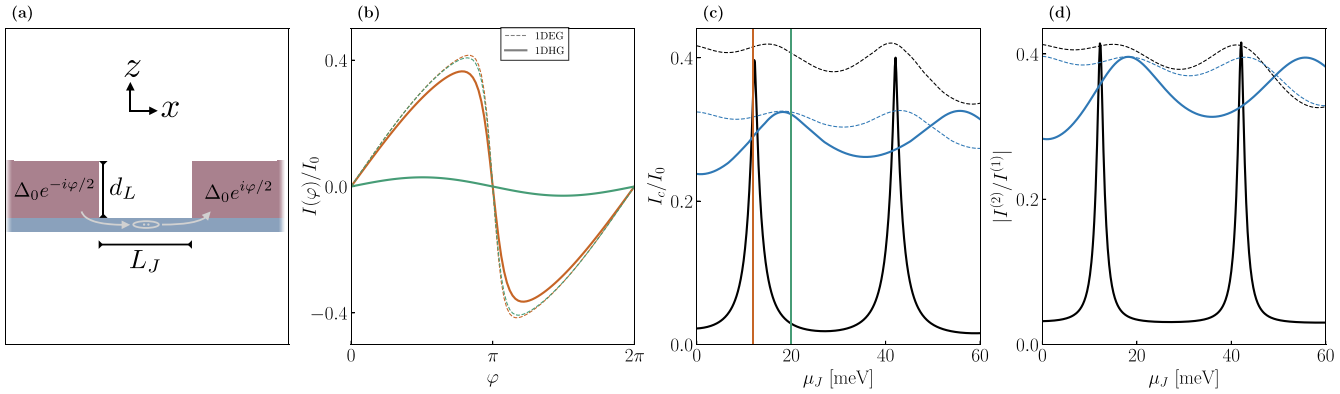

FIG. 3. One-dimensional JJ consisting of an infinite 1D semiconducting wire (blue), with a single subband that extends through both the junction region and the leads. Each lead is covered by a semi-infinite SC film (brown) with a phase difference φ across the JJ that generates a supercurrent $I(\varphi)$ in the wire. When the leads are in the insulating regime (black lines), the critical current I_c [panel (c)] and the ratio between the first two harmonics of the CPR, $|I^{(2)}/I^{(1)}|$, [panel (d)] are strongly nonmonotonic: Adjusting the chemical potential μ_J in the junction reveals sharp peaks in I_c and $|I^{(2)}/I^{(1)}|$ [see panels (c) and (d)], corresponding to bound states confined around the normal junction region. In contrast, for a 1DEG coupled to a superconductor [dashed lines in panels (c) and (d)] or when the 1DHG is in the SC phase [blue lines in panels (c) and (d)], the system exhibits a more steady dependence of I_c and $|I^{(2)}/I^{(1)}|$ on μ_J. In these cases, the oscillations are due to Andreev bound states whose transmissivity is μ_J dependent. The vertical lines in panel (c) show μ_J for the CPRs $I(\varphi)$ in panel (b) [$\mu_J = 12$ meV (orange) and 20 meV (green)]. The junction length is $L_J = 50$ nm, the superconductor thickness $d_L = 20$ nm, and the lattice constant $a = 0.5$ nm. Here, $k_B T = \Delta_0/20 \approx 100$ mK, $\mu_{\rm sm} = 90$ meV, and the hopping between the semiconductor and superconductor $t_c = 50$ meV (see Appendix D). For the black lines in panels (c) and (d) and all CPRs in panel (b) $\mu_{\rm sc} \approx 293$ meV, while for the blue lines in panels (c) and (d) $\mu_{\rm sc} \approx 306$ meV. The effective masses are the same as in Fig. 1. The supercurrents are normalized relative to $I_0 = |e|\Delta_0 \approx 49$ nA.

that is insulating, which is difficult to determine from the density of states alone or from the spectrum. However, when a supercurrent is forced through the semiconductor, as in a JJ, we can expect distinct signatures of insulating and SC phases (see below).

The resonances in Fig. 2(e), where the subband crossing occurs exactly at μ, arise approximately when $k_F d/\pi$ is an integer [as in Figs. 2(b) and 2(c)]. The insulating gap persists in an interval $\sim 2\gamma/\delta E_{\rm sc}$ around $k_F d/\pi$ (assuming $\Delta_0, \gamma \ll \delta E_{\rm sc}$). As such, increasing the coupling between the systems and/or the SC layer thickness will not only improve the proximity effect away from resonance (as discussed in Ref. [45] for 2DEGs) but will also make it more likely to be in an insulating phase. Numerically, we find that this behavior persists until $\gamma \gtrsim \delta E_{\rm sc}$, at which point the insulating phase starts to disappear and we obtain similar behavior as in Ref. [45] such that the SC proximity effect is more accurately described by the infinite superconductor limit (see Appendix C), and there is no difference in the proximity effect between 2DHGs and 2DEGs.

Surprisingly, by increasing γ a system being initially in the SC phase can be brought into the insulating phase for chemical potentials close to the crossing point [see Fig. 2(f)]. First, E_g increases as a function of γ for the 2DHG (thick line), so does the BCS charge $Q_g = |\langle k_g, E_g|\eta_z|k_g, E_g\rangle|$ (line color) (see Appendix A). The imbalance of the quasiparticle and quasihole components of the wave function leads to $Q_g \approx 1$, indicating a suppression of the SC proximity effect. Conversely, in the 2DEG case, E_g always represents the SC gap and thus approaches Δ_0 as $\gamma/\Delta_0 \gg 1$, with $Q_g \approx 0$ everywhere [thin lines in Figs. 2(d)–2(f)].

As discussed above, in this work we focus on the intermediate coupling regime, where $\Delta_0 \lesssim \gamma \ll \delta E_{\rm sc}$, such that we can obtain a large proximity effect even away from resonance but still only need to consider an individual subband in the superconductor. We note that this is the experimentally relevant regime because the SC pairing is usually $\Delta_0 \lesssim 1$ meV, while the subband spacing in metallic layers has a range $\delta E_{\rm sc} \sim$ 10–100 meV [60]. It is important to note that in this regime one also expects the largest differences between 2DHG and 2DEG hybrid systems with the insulating gap dominating over the SC proximity gap. As shown in Figs. 2(d)–2(f), whether the coupling between the subsystems leads to an SC or insulating gap can strongly depend on the system parameters. In an experiment, it is impractical to vary d and k_F will be almost fixed. Therefore, upon fabricating a device, it is possible to end up close to a resonance and, with only a small variation of parameters, either obtain a large proximity-induced pairing or an insulating phase. Here, we treat the effective parameters such as γ, d, z_0, and $\mu_{\rm sm}$ as independent. However, for example, applying an electric field to the semiconductor can localize the semiconductor wave function closer to the interface to the superconductor and this can increase γ, change $\mu_{\rm sm}$ as well as influence the effective lengths d and z_0.

III. ATYPICAL JOSEPHSON EFFECT

We consider a 1D JJ, where the leads consist of a semiconductor (one subband) covered by a superconductor with finite width, while the junction region consists only of this semiconducting subband. A schematic of the setup is shown in Fig. 3(a). The system is modeled using a tight-binding Hamiltonian, which includes a junction region (in which only semiconducting sites are present) and two infinite leads. Following Refs. [68–71] and using kwant [72], we numeri-

cally evaluate the supercurrent $I(\varphi)$ as function of the phase difference φ across the JJ.

To calculate the supercurrent through the junction, we use a Green's function approach, which is described in Refs. [68–71]. We attach virtual leads at two adjacent sites (sites m and $m+1$) in the junction and calculate the following quantity:

$$I_{m,m+1}(\varphi) = |e|k_BT \sum_{n=0}^{\infty} \mathrm{Im}\{\mathrm{Tr}[\eta_z H_{m,m+1} G_{m+1,m}(i\omega_n, \varphi) - \eta_z H_{m+1,m} G_{m,m+1}(i\omega_n, \varphi)]\}, \quad (8)$$

which describes the current between sites m and $m+1$. Here, e denotes the elementary charge, k_B is Boltzmann's constant, and T is the temperature of the system, which is taken to be significantly smaller than Δ_0/k_B. Here, $H_{m,m+1}$ is the matrix element of the tight-binding Hamiltonian that couples sites m and $m+1$ (hopping), while $G_{m,m+1}(i\omega_n, \varphi)$ is the Green's function matrix element that couples the same sites evaluated at the (fermionic) Matsubara frequency $i\omega_n$ (see Appendix D for further details).

As discussed above, the leads can be in the insulating phase for the semiconducting subband, which could suppress proximity-induced superconductivity. Consequently, the critical supercurrent I_c is strongly suppressed since other high-momentum superconducting subbands have a relatively small weight in the semiconductor such that they do not couple strongly to the normal semiconducting region. To illustrate this suppression, we plot I_c as a function of the chemical potential μ_J in the junction both inside and outside the insulating regime for the leads [see Fig. 3(c)]. As expected, near the insulating phase [Fig. 3(c)], I_c for 1DHGs (full line) is significantly suppressed compared to 1DEGs (dashed line). Notably, in this parameter regime, the hole system only exhibits a substantial I_c when a bound state forms in the normal region at an energy within the parent SC gap Δ_0, leading to a highly atypical Josephson effect—the junction behaves similarly to a dot-junction, despite being in a parameter regime where the transmission is expected to be close to unity. This is evident from the current peaks observed in Fig. 3(c). We note that the sharp peaks in I_c versus μ_J remain, even when the standard deviation of the chemical potentials (due to disorder) exceeds Δ_0 (see Appendix D). This confirms that the proposed effects are robust to disorder.

We note that the hopping strength t_c between the superconducting and semiconducting subsystems in Fig. 3 is chosen to be comparable to the subband spacing in the superconductor. As a result, several superconducting subbands contribute to the supercurrent. This indicates that the supercurrents shown in Fig. 3 persist even in the absence of pairing in the particular superconducting subband that undergoes the anticrossing with the hole band and is therefore gapped out by the insulating gap. This further highlights the necessity of explicitly including all superconducting subbands in the analysis.

Similarly, in Fig. 3(d), we show the ratio of the first two Fourier components of the current-phase relation (CPR) $I(\varphi) = \sum_{n=1}^{\infty} I^{(n)} \sin(n\varphi)$, with φ being the superconducting phase difference across the JJ, both inside and outside the insulating phase. Here, $I^{(n)}$ denotes the coefficient of the nth harmonic in the Fourier expansion of the CPR. These results further highlight a strong suppression of transparency in the insulating phase [73–75]. Finally, away from the insulating regime [blue lines in Figs. 3(c) and 3(d)], the atypical Josephson effect disappears, and both 1DHG (solid) and 1DEG (dashed) systems exhibit similar critical current and transparency behavior.

We conclude by noting that the effects discussed here are robust against moderate disorder, e.g., variations in chemical potential. As such, the atypical behavior uncovered in this work is not only of fundamental importance but also of key relevance in hybrid systems, such as proximitized Ge hole semiconductors, which are of significant current experimental interest [31,32,54–61].

ACKNOWLEDGMENTS

We would like to thank Joel Hutchinson, Maximilian Hünenberger, and Christoph Adelsberger for useful discussions. This work was supported by the Swiss National Science Foundation (SNSF) and NCCR SPIN (Grants No. 51NF40-180604 and No. 51NF40-225153).

DATA AVAILABILITY

The data that support the findings of this article are openly available [76].

APPENDIXES

In these Appendixes, we provide details on the analytic expressions used to describe the SC proximity effect for a 2DHG. First, we describe the Green's function approach and give explicit expressions for the various terms in the self-energy. Moreover, we describe the numerical methods used to create Figs. 1 and 2. Having established the Green's function description, we give a brief analysis on the effects of disorder and demonstrate that the main results in this work are robust against weak disorder. This is followed by a brief discussion on the effective size of the insulating gaps, which tells us about the probability of a system being in the insulating phase. We continue by discussing the limit where the superconductor has infinite length—a limit in which it does not matter whether the carriers in the semiconductor are holes or electrons. Additionally, we provide further details on the "effective two-band model," and how this can be used to calculate expressions for the pair expectation value in the semiconductor. Additionally, the two-band model allows us to estimate the size of the insulating gap given any ratio of effective masses. Finally, we present the numerical calculation of the supercurrent through a one-dimensional Josephson junction.

APPENDIX A: DYSON EQUATION

In this Appendix, we will give the expression used for the full Green's function of the semiconductor, after integrating out the SC layer of thickness d. This result is used to obtain Fig. 2.

Let us begin by defining the action that describes the s-wave SC [45]:

$$S_{\rm sc} = \frac{1}{2}\int_{k,\omega}\int_0^d \mathrm{d}z\, \boldsymbol{d}^\dagger_{k,\omega,z}(i\omega - H_{{\rm sc},k,z})\boldsymbol{d}_{k,\omega,z},$$
$$\int_{k,\omega}\cdots = \int_{\mathbb{R}^2}\frac{\mathrm{d}^2\boldsymbol{k}}{(2\pi)^2}\int_{-\infty}^{\infty}\frac{\mathrm{d}\omega}{2\pi}\cdots \tag{A1}$$

where $\boldsymbol{d}^\dagger_{k,\omega,z} = (d^\dagger_{k,\omega,z,\uparrow}, d_{-k,-\omega,z,\downarrow})$. The operator $d^\dagger_{k,\omega,z,\sigma}$ creates an electron with in-plane momentum $k = (k_x^2 + k_y^2)^{1/2}$ and Matsubara frequency ω at position z inside the superconductor (z denotes the position in the out-of-plane direction, and hence is constrained to lie between 0 and d). The fermionic Matsubara frequency is given by $\omega = i(2n+1)\pi k_B T$, where n is an integer, k_B is the Boltzmann constant, and T is the temperature (we set $\hbar = 1$ throughout). However, for Fig. 2, we take the zero temperature limit, which implies that we perform the analytical continuation $i\omega \to \omega + i0^+$, and obtain expressions that are in terms of the retarded Green's functions. Additionally, $H_{{\rm sc},k,z}$ is the Hamiltonian of the SC system:

$$H_{{\rm sc},k,z} = \left(\frac{k^2 - \partial_z^2}{2m_{\rm sc}} + V(z) - \mu_{\rm sc}\right)\eta_z + \Delta_0\eta_x, \tag{A2}$$

where $\eta_{x,y,z}$ are the Pauli matrices in Nambu space. $V(z)$ is assumed to be a hard-wall confinement, constraining the SC wave function to lie between $z = 0$ and $z = d$.

Similarly, the action that describes the 2DHG and 2DEG is given by

$$S_{\rm sm} = \frac{1}{2}\int_{k,\omega}\boldsymbol{c}^\dagger_{k,\omega}(i\omega - H_{{\rm sm},k})\boldsymbol{c}_{k,\omega}, \tag{A3}$$

where $\boldsymbol{c}^\dagger_{k,\omega} = (c^\dagger_{k,\omega,\uparrow}, c_{-k,-\omega,\downarrow})$ creates a spinor in the semiconductor and $H_{{\rm sm},k} = (k^2/2m_{\rm sm} - {\rm sgn}(m_{\rm sm})\mu_{\rm sm})\eta_z$ is the Hamiltonian of the 2DHG (2DEG). We restrict the semiconductor to its lowest subband, justified by the large confinement-induced level spacing along the z direction of the quasi-two-dimensional structure in the xy plane.

Finally, the coupling between the superconductor and the semiconductor is given by

$$S_c = -\frac{t_0}{2}\int_{k,\omega}\left(\boldsymbol{d}^\dagger_{k,\omega,z=z_0}\eta_z\boldsymbol{c}_{k,\omega} + \text{H.c.}\right), \tag{A4}$$

where t_0 is the coupling amplitude (with units of energy $\times$ $\sqrt{\text{length}}$), and where we assume that the semiconductor is positioned at $z = z_0$, which implies that the coupling only occurs at the interface at $z = z_0$. Due to the hard-wall boundary conditions, the SC Green's function vanishes exactly at $z = 0$, necessitating that $z_0 > 0$. In Fig. 2 and in the main text, we set $z_0 = \lambda_F/7$, where $\lambda_F \approx 0.35$ nm is the Fermi wavelength of the SC.

Following the calculation in Ref. [45], we solve the Dyson equation for the hybrid SC-semiconductor system, which gives us the full Matsubara Green's function of the system

$$G_{k,\omega} = (i\omega - H_{{\rm sm},k} - \Sigma_{k,\omega})^{-1}. \tag{A5}$$

The results in this section are independent of the exact expression for $H_{{\rm sm},k}$ and, therefore, are equally valid for 2DHGs and 2DEGs.

The Green's function and Hamiltonian are in the BdG basis: $\psi^\dagger_k = (c^\dagger_{\uparrow k}, c_{\downarrow -k})$, where $c^\dagger_{\sigma k}$ creates a hole (electron) with spin σ and momentum k in the 2DHG (2DEG). Spin is a good quantum number because we are studying systems without spin-orbit coupling and, as such, we can represent the system in terms of 2×2 Green's functions/Hamiltonians. The self-energy $\Sigma_{k,\omega}$ can be decomposed into the Pauli representation [as in Eq. (4)],

$$\Sigma_{k,\omega} = (i\omega - \Delta_0\eta_x)(1 - \Gamma^{-1}_{k,\omega}) - \delta\mu_{k,\omega}\eta_z. \tag{A6}$$

The functions $(1 - \Gamma^{-1}_{k,\omega})$ and $\delta\mu_{k,\omega}$ have simple poles at the energy levels of the SC. As described in Ref. [45], they can be expressed as

$$\Gamma_{k,\omega} = \left(1 + \frac{\gamma}{\Omega\varphi[\cosh(2\chi d) - \cos(2\zeta d)]}\{\sinh(2\chi d) - \cos(2\zeta z_0)\sinh[2\chi(d - z_0)] - \cos[2\zeta(d - z_0)]\sinh(2\chi z_0)\}\right)^{-1},$$
$$\delta\mu_{k,\omega} = -\frac{\gamma}{\varphi[\cosh(2\chi d) - \cos(2\zeta d)]}\{\sinh(2\zeta d) - \sin(2\zeta z_0)\cosh[2\chi(d - z_0)] - \sin[2\zeta(d - z_0)]\cosh(2\chi z_0)\}, \tag{A7}$$

where we define

$$\varphi = \sqrt{1 - k^2/k_F^2}, \quad \zeta = k_F\varphi,$$
$$\Omega = \sqrt{\Delta_0^2 + \omega^2}, \quad \chi = 2m_{\rm sc}\Omega/\zeta, \quad \gamma = t_0^2/v_F. \tag{A8}$$

The lower boundary of the SC layer is located at $z = 0$, while the 2DH(E)G is located at $z = z_0$ for $0 \leqslant z_0 \leqslant d$. Here, v_F denotes the Fermi velocity of the SC.

The dispersion relations, $E(k)$, used in the main text are then obtained by solving the generalized eigenvalue problem

$$[E^+(k) - H_{{\rm sm},k} - \Sigma_{k,E^+(k)}]\psi_{k,E^+(k)} = 0, \tag{A9}$$

where $E^+(k) = E(k) + i0^+$.

This is equivalent to finding the poles of the full retarded Green's function. Numerically, it is advantageous to find the zeros of $\det(E^+ - H_{{\rm sm},k} - \Sigma_{k,E^+})$ instead of the poles of the retarded Green's function G^R_{k,E^+}.

Effective quasiparticle weight in Figs. 2(a)–2(c). The effective quasiparticle weight can be calculated using

$$Z_{k,\omega} = \frac{1}{1 - \partial_\omega\left[\omega\left(1 - \Gamma^{-1}_{k,\omega}\right)\right]} = \frac{\Gamma^2_{k,\omega}}{\Gamma_{k,\omega} - \omega\partial_\omega\Gamma_{k,\omega}}. \tag{A10}$$

When $Z_{k,\omega} = 1$, the pole of the full Green's function describes a state that has all its weight in the semiconductor, whereas for $Z_{k,\omega} = 0$ the Green's function poles describe states in the

SC. This is used in Figs. 2(a)–2(c) to show the weight of each subband in the SC.

BCS charge in Figs. 2(d)–2(f). Having found the dispersion $E(k)$, as described above, we can evaluate the effective Hamiltonian, which is defined as

$$H_{\text{eff}} = H_{\text{sm},k} + \Sigma_{k,E(k)}. \tag{A11}$$

More specifically, for Figs. 2(d)–2(f), we evaluate H_{eff} at the energy minimum E_g (and the corresponding momentum k_g) as well as find corresponding wave functions:

$$H_{\text{eff}}(k_g, E_g)|k_g, E_g\rangle = E_g|k_g, E_g\rangle. \tag{A12}$$

Using $|k_g, E_g\rangle$, we evaluate the expectation value of η_z, which will give us an estimate for the BCS charge:

$$Q_g \equiv |\langle k_g, E_g|\eta_z|k_g, E_g\rangle| \tag{A13}$$

at the edge of the bulk band. If $Q_g = 0$, the wave function consists of equal parts quasiparticle and quasihole. Thus, one is in the superconducting phase. In our work, $Q_g \to 1$ implies that the wave function is of purely electron or hole character. Thus, one is in the insulating gap. The Q_g values are shown by colors in Figs. 2(d)–2(f)—we see that when $E_g < \Delta_0$ the value $Q_g \approx 0$; however, as soon as $E_g > \Delta_0$ the quantity Q_g starts to increase and approach unity.

1. Insulating gaps in the presence of weak disorder

An important aspect of proximitized superconductivity is disorder, which unavoidably will be present in realistic systems. Specifically, it is the disorder in the SC, which can play an important role for our results because it can broaden the self-energy. Here, we briefly comment on the effect that disorder in the SC layer will have on the results in this work.

The impact of disorder on the density of states (DOS) is evidenced by the broadening of the energy peaks within the system. In this Appendix, we characterize this broadening by incorporating a constant imaginary self-energy into the SC Green's function. This approach enables us to provide a general overview of the effects of disorder on the system, despite the fact that momentum is no longer a valid quantum number. It is important to note that this technique captures only the broadening of the peaks in the DOS and does not fully account for the effects of disorder.

As we just described, we model the effect of disorder by the addition of a small imaginary self-energy $i\Lambda$ in the SC. This is achieved by setting $\omega \to \omega + i\Lambda$ in the self-energy in Eq. (A6). Using this, we can calculate the DOS in the semiconductor:

$$\rho_{k,\omega} = -\frac{2}{\pi}\text{Im}\{\text{tr}[(\omega + i0^+ - H_{\text{sm},k} - \Sigma_{k,\omega+i\Lambda})^{-1}]\}, \tag{A14}$$

where the factor two is due to the spin-degeneracy of the system. In particular, when the insulating gap is much larger than Δ_0, we need to compare the broadening to the insulating gap size. Thus, the insulating phase discussed in this work can be relevant even for a level broadening that surpasses the parent pairing potential Δ_0. To demonstrate this, in Fig. 4, we plot $\rho_{k,\omega}$ in momentum space. Even for cases where the level broadening is substantially larger than the parent pairing potential Δ_0 [see Figs. 4(d)– 4(f)], ρ is still suppressed for a range of energies, i.e., the insulating gap survives even in the presence of relatively strong disorder.

Hence, our analysis implies that the insulating gap physics discussed in the main text is still relevant in the presence of broadening, i.e., disorder, provided the coupling is strong. However, we still expect that this can only be seen in relatively clean systems, where the broadening is smaller than the subband spacing in the SC, i.e. where the mean-free path is larger than the thickness d of the SC layer.

2. Dependence of resonances on coupling strength and height of the SC

In this Appendix, we establish how the coupling strength γ, the thickness of the SC layer d and the SCs Fermi momentum k_F, affect the probability of a system being in the insulating phase. In particular, we are interested in regions of parameter space, where the gap in the 2DHG is *larger* than Δ_0. The nth subband energy in a confined metallic system of height d with a parabolic dispersion (as in our SC layer) is given by

$$E_n(d) = \frac{\pi^2 n^2}{2md^2} - E_F, \tag{A15}$$

where E_F denotes the Fermi energy and n is the subband index. To estimate the size of the resonances, we can calculate the length scale by which d needs to change in order for the energy of the nth subband to vary by 2γ. To solve this, we can solve the following equation for $\delta d \geqslant 0$:

$$-[E_n(d + \delta d/2) - E_n(d - \delta d/2)] = 2\gamma, \tag{A16}$$

since this gives us an approximate range in height d, where the system is close to resonance. By evaluating the above expression, we obtain

$$\frac{16d\pi^2 n^2 \delta d}{m(\delta d^2 - 4d^2)^2} = 2\gamma. \tag{A17}$$

Since we assume the change in height is smaller than the total height, $\delta d \ll d$, we can expand the left-hand side to linear order in δd, giving

$$\delta d \approx \frac{2m\gamma d^3}{n^2\pi^2}. \tag{A18}$$

Furthermore, the subband index is given by $n = \lfloor k_F d/\pi \rfloor$, and thus we can write

$$\frac{k_F \delta d}{\pi} \approx \frac{2\gamma d}{\pi v_F} = \frac{2\gamma}{\delta E_{\text{sc}}}, \tag{A19}$$

where k_F and $\delta E_{\text{sc}} = \pi v_F/d$ are the Fermi momentum and subband spacing in the SC, respectively. Hence, the size of the resonances [e.g., in Fig. 2(d)] are proportional both to the coupling strength γ and to the thickness d of the SC layer. In agreement with this analytic derivation, we also find numerically that the insulating region becomes wider as we increase d or γ. Moreover, we see that when $\gamma/\delta E_{\text{sc}}$ becomes unity, we approach the regime in which neighboring resonances in Fig. 2(d) in the main text begin influencing one another.

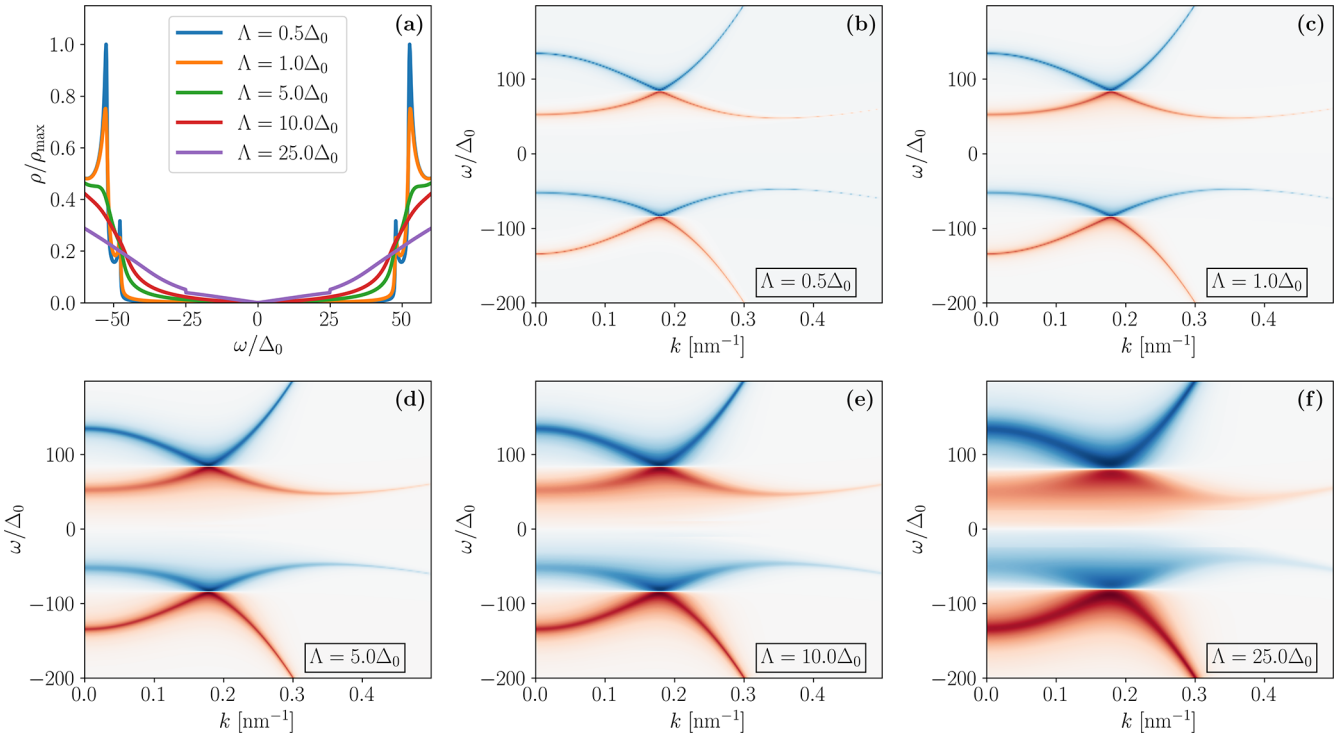

FIG. 4. The effect of disorder on the density of states $\rho_{k,\omega}$ in the semiconductor. Panel (a) shows the energy dependence of $\rho_{k,\omega}$ for different disorder strengths integrated over a small momentum range (0–0.5 nm^{-1}). Note that the peaks are due to the van Hove singularities at the edges of the insulating gaps, which accounts for the energy scale being much larger than the parent gap Δ_0. Panels (b)–(f) show the momentum dependent $f(\rho_{k,\omega})$ for the different disorder strengths, where $f(x) = \mathrm{sgn}(x)\log(1 + 5000|x|)$ is used to show the general behavior of the DOS, despite it being very peaked in panels (b) and (c). The disorder strengths in panels (b)–(f) are given by $\Delta_0/2$, Δ_0, $5\Delta_0$, $10\Delta_0$, and $25\Delta_0$, respectively. These are also the disorder strengths chosen in panel (a) and are shown by blue, yellow, green, red, and purple lines, respectively.

APPENDIX B: EFFECTIVE TWO-BAND MODEL

In this Appendix, we further examine the "effective two-band model" from the main text, which describes a single semiconducting subband coupled to a single SC subband. We will show that some of the effects discussed in the main text (such as the presence of a gap larger than Δ_0 and the suppression of the SC proximity effect in 2DHGs) can be understood in terms of exact expressions obtained in this section. We discuss them graphically in Fig. 5.

We will begin by discussing the normal spectrum of the effective two-band model, which is given by the Hamiltonian

$$H_{N,\sigma,k} = \xi_{\mathrm{sc},k} d^\dagger_{\sigma,k} d_{\sigma,k} + \xi_{\mathrm{sm},k} c^\dagger_{\sigma,k} c_{\sigma,k} + t d^\dagger_{\sigma,k} c_{\sigma,k} + t c^\dagger_{\sigma,k} d_{\sigma,k}, \tag{B1}$$

where $d^\dagger_{\sigma,k}$ creates an electron in the superconductor with momentum k and spin σ, and $c^\dagger_{\sigma,k}$ creates a hole (electron) in the 2DHG (2DEG) with momentum k and spin σ. Additionally, $\xi_{n,k} = k^2/(2m_n) - \mathrm{sgn}(m_n)\mu_n$ denotes the kinetic energy of subband n, minus the effective chemical potential, $\mu_n \in \{\mu_{\mathrm{sm}}, \bar{\mu}_{\mathrm{sc}}\}$, and t is the effective coupling between the subbands (and thus has units of energy). We can represent this by the following 2×2 Hamiltonian:

$$H_{N,\sigma,k} = \begin{pmatrix} \xi_{\mathrm{sm},k} & t \\ t & \xi_{\mathrm{sc},k} \end{pmatrix} \tag{B2}$$

in the $(c^\dagger_{k,\sigma}, d^\dagger_{k,\sigma})$ basis.

Using the Hamiltonian $H_{N,\sigma,k}$ in Eq. (B2), we can calculate the dispersion relation of the coupled system without superconductivity. This is used to obtain Figs. 1(c) and 1(d). In the context of the SC proximity effect, we are especially interested in parameters where $H_{N,\sigma,k}$ has a zero eigenvalue and there is a crossing between two subbands around zero energy. This occurs when $\xi_{\mathrm{sm},k} = g(\xi_{\mathrm{sc},k}) \equiv t^2/\xi_{\mathrm{sc},k}$.

Moreover, the weight in the semiconductor $|\psi_{\mathrm{sm}}|^2$ can be defined in terms of the above quantities:

$$|\psi_{\mathrm{sm}}|^2 = \frac{1}{2}(1 \pm \sin\phi), \quad \phi = \arctan\left(\frac{\xi_{\mathrm{sc},k} - \xi_{\mathrm{sm},k}}{2t}\right), \tag{B3}$$

which is used in Figs. 1(c) and 1(d) to color the subbands. Note that this quantity is closely related to $Z_{k,\omega}$ [Eq. (A10)], as they both contain information about the wave function weight in the semiconductor; however, in this Appendix we consider only a single subband in the superconductor, while $Z_{k,\omega}$ describes the weight in the semiconductor after integrating out the full superconductor.

Finally, the size of the insulating gap in the spectrum can be calculated by requiring that the effective masses/Fermi velocities have opposite signs, and is given by $2\Delta_{\mathrm{ins}}$:

$$\Delta_{\mathrm{ins}} = \frac{2t\sqrt{|v_{\mathrm{sc}} v_{\mathrm{sm}}|}}{|v_{\mathrm{sc}}| + |v_{\mathrm{sm}}|} = \frac{2t\sqrt{|m_{\mathrm{sc}} m_{\mathrm{sm}}|}}{|m_{\mathrm{sc}}| + |m_{\mathrm{sm}}|}, \tag{B4}$$

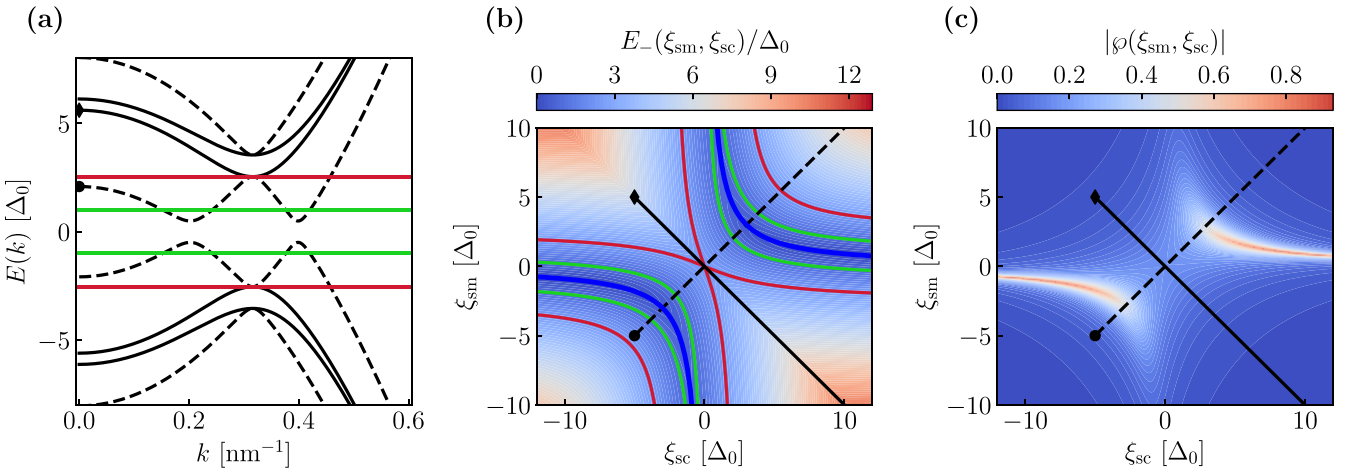

FIG. 5. Suppression of the SC proximity effect in 2DHGs close to the resonance (with the chemical potential being close to the crossing point between semiconducting and superconducting subbands). The corresponding energy spectrum is shown in panels (a) and (b), as well as the proximity-induced pair expectation value in panel (c). We demonstrate the differences between systems with Fermi velocities of equal signs (dashed lines) and opposite signs (solid lines). Not only do the gap sizes [which can be read off in panels (a) and (b)] differ, but also the pair expectation values [shown in panel (c)] depend strongly on the relative signs of the Fermi velocities and on the chemical potentials in the subsystems. This again shows that the insulating gaps in 2DHGs can suppress the SC proximity effect. The smallest energy in the spectrum of H_k, $E_-(\xi_{\mathrm{sc},k}, \xi_{\mathrm{sm},k})$, takes smallest values along the curve $\xi_{\mathrm{sm},k} = g(\xi_{\mathrm{sc},k}) = t^2/\xi_{\mathrm{sc},k}$. It is generally larger than Δ_0 [green contour in panel (b), and green horizontal line in panel (a)] and exceeds $E_{g,\max}$ [red contour in panel (b) and line in panel (a)] in the second and fourth quadrant. The straight line $(\xi_{\mathrm{sc},k}, \xi_{\mathrm{sm},k})$ is forced to cross the curve $g(\xi_{\mathrm{sc},k})$ if the effective masses have the same sign [see the dashed lines in panels (b) and (c)], whereas it can avoid the $E_- < \Delta_0$ region completely if effective masses have opposite signs. Similarly, the pair expectation value, $\wp$ defined in Eq. (B10), is suppressed away from $g(\xi_{\mathrm{sc},k})$, as is seen in panel (c). Here, the magnitudes of Fermi velocities are set equal and $t = 3\Delta_0$ and $\Delta_0 = 0.2\,\mathrm{meV}$. For further details, see Appendix B.

where v_{sc} (m_{sc}) and v_{sm} (m_{sm}) are the Fermi velocities (effective masses) of the SC and semiconducting subbands, respectively, and t is the coupling between the subbands.

Introducing the SC pairing potential (Δ_0), and going to the BdG description, we obtain the following Hamiltonian:

$$H_k = \begin{pmatrix} \xi_{\mathrm{sm},k} & t & 0 & 0 \\ t & \xi_{\mathrm{sc},k} & 0 & \Delta_0 \\ 0 & 0 & -\xi_{\mathrm{sm},k} & -t \\ 0 & \Delta_0 & -t & -\xi_{\mathrm{sc},k} \end{pmatrix}, \tag{B5}$$

in the basis $(c^\dagger_{k,\uparrow}, d^\dagger_{k,\uparrow}, c_{-k,\downarrow}, d_{-k,\downarrow})$.

The positive energy spectrum of H_k is given by

$$E_\pm(\xi_{\mathrm{sm},k}, \xi_{\mathrm{sc},k}) = \frac{1}{2}\sqrt{2t^2 + \Delta_0^2 + \xi^2_{\mathrm{sc},k} + \xi^2_{\mathrm{sm},k} \pm \sqrt{4t^2\left[\Delta_0^2 + (\xi_{\mathrm{sc},k} + \xi_{\mathrm{sm},k})^2\right] + \left(\Delta_0^2 + \xi^2_{\mathrm{sc},k} - \xi^2_{\mathrm{sm},k}\right)^2}}. \tag{B6}$$

The negative eigenvalues are given by $-E_\pm$, as required by particle-hole symmetry. We introduce $E_\pm$ as a function of $\xi_{\mathrm{sm},k}$ and $\xi_{\mathrm{sc},k}$ as parametrizing everything in terms of $\xi_{\mathrm{sm},k}$ and $\xi_{\mathrm{sc},k}$ simplifies the calculations compared to using chemical potentials and momenta separately.

In the SC system, the curve $\xi_{\mathrm{sm}} = g(\xi_{\mathrm{sc},k}) = t^2/\xi_{\mathrm{sc},k}$ approximately describes the local minima in the energy E_-. This approximate description is valid for $t \gtrsim \Delta_0$. In Fig. 5(b), we show the smallest positive eigenvalue of H_k, E_-, as a function of $\xi_{\mathrm{sc},k}$ and $\xi_{\mathrm{sm},k}$. Additionally, we add the line $g(\xi_{\mathrm{sc},k}) = t^2/\xi_{\mathrm{sc},k}$ (blue) and the contour $E_- = \Delta_0$ (green). Furthermore, we can parametrize the lines $(\xi_{\mathrm{sc},k}, \xi_{\mathrm{sm},k})_k$ in terms of straight lines in the $\xi_{\mathrm{sc},k}$–$\xi_{\mathrm{sm},k}$ plane. These lines are described by

$$\xi_{\mathrm{sm},k}(\xi_{\mathrm{sc},k}) = \frac{m_{\mathrm{sc}}}{m_{\mathrm{sm}}}(\xi_{\mathrm{sc},k} + \bar{\mu}_{\mathrm{sc}}) - \mu_{\mathrm{sm}}. \tag{B7}$$

Thus, we see that $\xi_{\mathrm{sm},k}(\xi_{\mathrm{sc},k})$ is an increasing function in $\xi_{\mathrm{sc},k}$, when the sign of the effective masses are equal, and that $\xi_{\mathrm{sm},k}(\xi_{\mathrm{sc},k})$ will always cross the curve $g(\xi_{\mathrm{sc},k}) = t^2/\xi_{\mathrm{sc},k}$. Whereas, when the signs are opposite, there exist combinations of chemical potentials, for which $\xi_{\mathrm{sm},k}(\xi_{\mathrm{sc},k})$ can avoid the line $g(\xi_{\mathrm{sc},k})$. These are the resonances discussed in the main text at which the gap E_g can be larger than Δ_0.

1. Pair expectation value

Using the Hamiltonian defined in Eq. (B5), we can calculate the pair expectation value of the ground state. The operator that describes the pairing in the semiconducting

subband, expressed in the same basis as H_k is given by

$$P = \begin{pmatrix} 0 & 0 & 1 & 0 \\ 0 & 0 & 0 & 0 \\ 1 & 0 & 0 & 0 \\ 0 & 0 & 0 & 0 \end{pmatrix}, \tag{B8}$$

and we define the pair expectation value as $\wp = \sum_{E<0}\langle E|P|E\rangle$, where $|E\rangle$ is the eigenfunction at energy E. We now calculate the residue of the Green's function, $G^R(\omega) = (\omega - H_k + i0^+)^{-1}$, at the two negative eigenvalues. This is related to the expectation value by

$$\wp = \sum_{E\in\{-E_-,-E_+\}} \lim_{\omega\to E}(\omega - E)\mathrm{tr}[G^R(\omega)P]. \tag{B9}$$

By expressing G^R in terms of the eigenvalues of H_k, we can calculate $\wp$ exactly and express it in terms of $E_\pm$:

$$\wp = \frac{-2t^2\Delta_0}{E_-E_+(E_+ + E_-)}. \tag{B10}$$

In Fig. 5(c), $\wp(\xi_{\mathrm{sm},k}, \xi_{\mathrm{sc},k})$ is shown, demonstrating that the pair expectation value is maximal around $g(\xi_{\mathrm{sc},k})$, which tells us that proximity-induced superconductivity is suppressed in the insulating phase [when $\xi_{\mathrm{sm},k}(\xi_{\mathrm{sc},k})$ can avoid crossing the $g(\xi_{\mathrm{sm},k})$ line]. We note that the expression for $\wp$ obtained from the residue of G^R is equivalent to one obtained by evaluating the expectation value of the pairing operator using the eigenstates of H_k. However, it has the benefit that it can easily be rewritten in terms of $E_\pm$.

To gain a better understanding of $\wp$, we can consider the two limiting cases, where the ratio between effective masses is $m_{\mathrm{sm}}/m_{\mathrm{sc}} = \pm 1$. For $m_{\mathrm{sm}}/m_{\mathrm{sc}} = 1$, we obtain an approximate expression for $\wp$, such that

$$|\wp_{\max}| \approx \frac{1}{2} - \frac{\Delta_0}{8t} + \mathcal{O}\left(\frac{\Delta_0^2}{t^2}\right), \quad \text{for } t \gg \Delta_0. \tag{B11}$$

However, for $m_{\mathrm{sm}}/m_{\mathrm{sc}} = -1$, we obtain an exact expression for the maximal $\wp$ at $\xi_{\mathrm{sc},k} = \xi_{\mathrm{sm},k} = 0$, such that

$$|\wp(0,0)| = \frac{\Delta_0}{\sqrt{4t^2 + \Delta_0^2}}. \tag{B12}$$

In this calculation, we have additionally assumed that $m_{\mathrm{sm}}\mu_{\mathrm{sm}} = m_{\mathrm{sc}}\bar{\mu}_{\mathrm{sc}}$. We see that increasing t can *reduce* the proximitized pair expectation value for 2DHGs, whereas $|\wp|$ will asymptotically approach $1/2$ in the electron case, as t is increased.

In Fig. 5(a), we show the full dispersions for systems $m_{\mathrm{sm}}/m_{\mathrm{sc}} = 1$ (dashed lines) and $m_{\mathrm{sm}}/m_{\mathrm{sc}} = -1$ (solid lines). We see that whilst the gap for $m_{\mathrm{sm}}/m_{\mathrm{sc}} = 1$ is $E_g < \Delta_0$, we obtain $E_g = E_{g,\max} > \Delta_0$ for $m_{\mathrm{sm}}/m_{\mathrm{sc}} = -1$, where

$$E_{g,\max} = \frac{1}{2}\left(\sqrt{4t^2 + \Delta_0^2} - \Delta_0\right). \tag{B13}$$

$E_{g,\max}$ is shown by the red contours in Fig. 5(b). We consider $t > \sqrt{2}\Delta_0$, therefore $E_{g,\max} > \Delta_0$.

2. Mass dependence of the insulating gap

In realistic systems, the effective masses/Fermi velocities in the semiconductor and superconductor will have different magnitudes. As discussed previously, this can make the insulating gaps smaller. This effect can already be seen from the normal spectrum, where the insulating gap of the size $2\Delta_{\mathrm{ins}}$ is opened at the crossing between two subbands:

$$\Delta_{\mathrm{ins}} = \frac{2t\sqrt{|m_{\mathrm{sc}}m_{\mathrm{sm}}|}}{|m_{\mathrm{sc}}| + |m_{\mathrm{sm}}|} = \frac{2t\sqrt{|r|}}{1+|r|}, \tag{B14}$$

where m_{sc} and m_{sm} are the effective masses of the SC and semiconducting subbands respectively. The renormalization depends only on the ratio between two masses, $r = m_{\mathrm{sm}}/m_{\mathrm{sc}}$. For linearized spectra, $r = v_{\mathrm{sc}}/v_{\mathrm{sm}}$ instead. For the parameters used in this work (see the caption of Fig. 1), this results in a reduction of the insulating gap in the normal spectrum, $2\Delta_{\mathrm{ins}}$, by approximately a factor of two, compared to the case in which the effective masses have equal magnitudes.

The insulating gap $2\Delta_{\mathrm{ins}}$ in the spectrum results in an excitation gap in the normal spectrum, E_g, which depends on the chemical potential. The largest E_g is observed as the chemical potential is tuned in the middle of the insulating gap, opened at the crossing point between semiconducting and superconducting subbands, and is given by Δ_{ins}. In the presence of superconductivity, we also expect that the gap in the SC spectrum will be affected by the difference in effective masses. Here, we assume that the chemical potential is tuned at the crossing point between semiconducting and superconducting subbands (this gives us an upper bound for E_g, which we call $E_{g,\max}$). To calculate this quantity, we set $\xi_{\mathrm{sc}} = r\xi_{\mathrm{sm}}$ (under this condition the uncoupled subbands meet at the chemical potential) in Eq. (B6) and minimize E_- with respect to ξ_{sm}. We obtain the following expression for the E_g in the BdG spectrum:

$$E_{g,\max,r}(r,t,\Delta_0) = \begin{cases} E_{g,\max}(t,\Delta_0), & \text{for } r_- < r < r_+, \\ E_{g,\mathrm{md}}(r,t,\Delta_0), & \text{otherwise,} \end{cases} \tag{B15}$$

where for small $\chi \equiv \Delta_0/t$:

$$r_\pm \approx -1 \pm \sqrt{2\chi} + \mathcal{O}(\chi), \tag{B16}$$

and the mass-dependent gap is given by

$$E_{g,\mathrm{md}}(r,t,\Delta_0) \approx \begin{cases} t\left(\frac{2\sqrt{|r|}}{1+|r|} + \mathcal{O}[\chi^2]\right), & \text{for } r \leqslant r_- \text{ or } r_+ \leqslant r < 0; \\ \Delta_0\left(\frac{1}{1+r} + \mathcal{O}[\chi^2]\right), & \text{for } \max\{0, r_+\} \leqslant r, \end{cases} \tag{B17}$$

for $t \gg \Delta_0$.

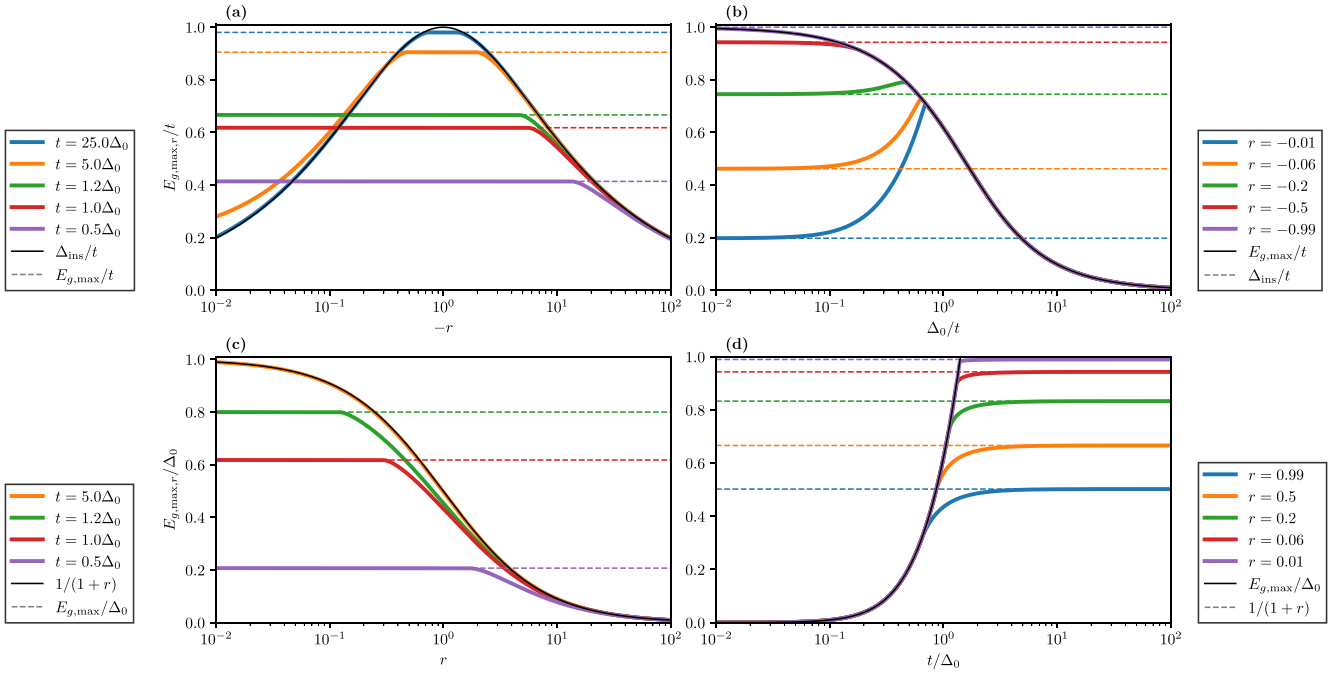

FIG. 6. The largest mass-dependent gap obtained from the two-band model [see Eqs. (B15)–(B17)] when the chemical potential is tuned to the crossing points between the semiconducting and superconducting subbands [panels (a) and (c)] for different values of t/Δ_0 as a function of r and [panels (b) and (d)] for different values of r as a function of t/Δ_0. For negative r [panels (a) and (b)], the energies are normalized relative to t, whereas for positive r [panels (c) and (d)], the energies are normalized to Δ_0. The dashed lines in panel (a) show the value of $E_{g,\max}/t$, which describes the value at the plateaus. The dashed lines in panel (c) show the value of $E_{g,\max}/\Delta_0$, which is only the limit value for large r, provided that $t \leqslant \sqrt{2}\Delta_0$. In panels (b) and (d), the dashed lines show the asymptotic limit as $t/\Delta_0 \gg 1$, which for panel (b) is given by $\Delta_{\rm ins}/t$, but for panel (d) is determined purely by the mass ratio: $1/(1+r)$. For $|r| < 1$, the excitation gap is given by $E_{g,\max}$ for $t \lesssim \Delta_0$, whereas for $t \gtrsim \Delta_0$ it is given by $\Delta_0/(1+r)$ ($\Delta_{\rm ins}$) for r positive (negative).

As can be seen in Fig. 6, there are three energy scales that are relevant in the system: $E_{g,\max}$, $\Delta_{\rm ins}$, and $\Delta_0/(1+r)$. For $\chi \lesssim 1$, E_g is given by $\Delta_{\rm ins}$ for $r < 0$, whereas for $r > 0$ it is given by $\Delta_0/(1+r)$. In the opposite limit, where $\chi \gtrsim 1$, E_g is instead given by $E_{g,\max}$ for all r. For intermediate values of χ, E_g smoothly transitions between the two limits. For semiconductors being proximitized by metals, typically $|r| < 1$. Therefore, for $\chi \ll 1$, E_g is given by $\Delta_{\rm ins}$ for $r < 0$ and by $\Delta_0/(1+r)$ for $r > 0$. Hence, even if the difference in magnitudes of the effective masses is taken into account, it is clear that E_g can exceed Δ_0.

APPENDIX C: INFINITE SC

Here, we study the behavior of the SC proximity effect in the limit where the height of the superconductor becomes very large, i.e., $d \to \infty$. Physically, this limit corresponds to the regime $d \gg \xi_0$, where ξ_0 denotes the coherence length of the superconductor. As we will see, the difference between SC proximity effects in 2DHGs and 2DEGs will vanish in this limit.

In the $d \to \infty$ limit, the dimensionless proximity-induced gap $\epsilon = E_g/\Delta_0$ depends only on the ratio between the coupling and the parent gap, $x = \gamma/\Delta_0$. This can be shown by beginning with the expressions given in Eqs. (A6) and (A7), setting $z_0 = d/2$ and letting $d \to \infty$. The requirement that $z_0 = d/2$ is to ensure a constant effective coupling strength. This gives us a Matsubara self-energy that is independent of k (which also means there is no difference between the 2DHG and 2DEG in this limit):

$$\Sigma = -\frac{\gamma(i\omega - \Delta_0\eta_x)}{\sqrt{\Delta_0^2 + \omega^2}}, \tag{C1}$$

in accordance with Ref. [45]. Using this expression, we calculate the full Green's function $G = (i\omega - \xi\eta_z - \Sigma)^{-1}$, where $\xi = k^2/(2m_{\rm sm}) - \mu_{\rm sm}$. We now perform the analytical continuation $i\omega \to \omega + i0^+$, allowing us to find the induced gap. We can now require that the retarded Green's function diverges and evaluate the eigenenergy at $\xi = 0$ (Σ is independent of k, so this will give us the proximity-induced gap), and express it in terms of the dimensionless quantities defined above [47]:

$$[\epsilon(x)]^2\left(1 + \frac{2x}{\sqrt{1-[\epsilon(x)]^2}}\right) = x^2, \tag{C2}$$

where $x = \gamma/\Delta_0$ and $\epsilon = E_g/\Delta_0$. As a result, the dimensionless gap takes on the following form, for 2DHGs and 2DEGs alike:

$$\epsilon(x) = \frac{1}{\alpha(x)}\left(x^2 - \frac{1}{3}[\{\alpha(x)\}^2 + \alpha(x) + 1]\right), \tag{C3}$$

where $\alpha(x) = \eta(x)(1 - 18x^2 + 3\sqrt{3}x\sqrt{x^4 + 11x^2 - 1})^{1/3}$ and where $\eta(x \geqslant 1/\sqrt{3}) = 1$, whereas $\eta(x < 1/\sqrt{3}) = \exp(\frac{2\pi i}{3})$. Using this expression, we can derive the asymptotic behavior of the induced gap, $E_g \sim \Delta_0(1 - 2\Delta_0^2/\gamma^2)$ for

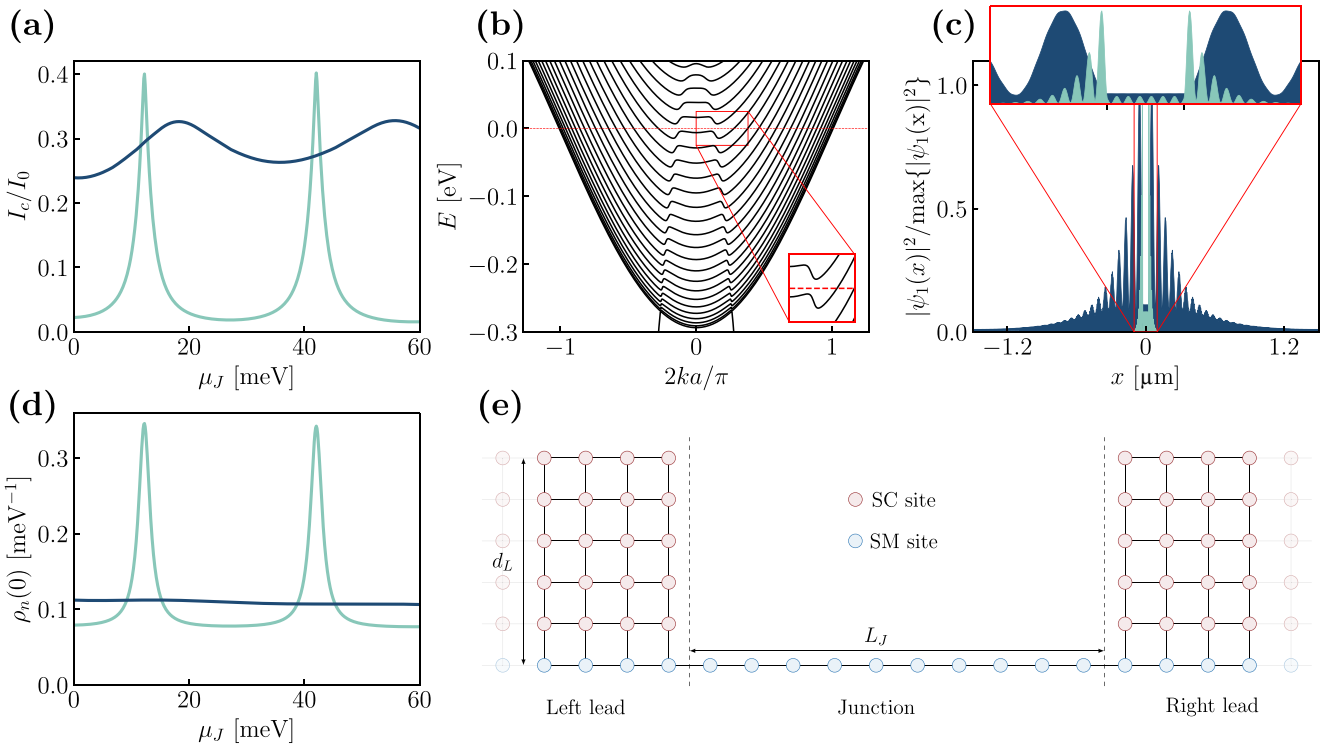

FIG. 7. In the insulating phase, the peaks in the critical current I_c [shown in panel (a), light blue] appear at the same values of μ_J as the peaks in $\rho_n(0)$ [shown in panel (d), light blue]; thus, these peaks can be attributed to bound states confined by the insulating gap in the normal section of the junction (present in the spectrum even in the absence of SC, $\Delta_0 = 0$). (c) The wave functions of these bound states (light blue) can be calculated in the two-subband tight-binding model assuming that the leads are longer than the coherence length of the superconductor [in panel (c) the junction extends from $x = -25$ to 25 nm, the ends of the junction are shown by the ticks on the inserted axis of panel (c)]. There is only one bound state with wave function $\langle x|\psi_1\rangle = \psi_1(x)$ in the considered regime. These bound states are localized on a length scale set by the insulating gap, which is much shorter than the coherence length of the SC part of the leads [compare to the typical ABS wave function shown in dark blue in panel (c)]. (b) In the normal state, the energy spectrum of leads contains several metallic electronic subbands (positive effective mass) and a single hole-semiconductor subband. The insulating gap is opened at anticrossings between the superconducting subbands and the hole-semiconducting subband, as can be seen from the insert in panel (b). (e) A sketch of the tight-binding chain used for the Josephson junction calculation. The leads consist of a single chain of semiconductor sites (blue) coupled of an SC strip of finite thickness d_L (red). The leads are semi-infinite in all calculations except for panel (c), where we consider only the lowest-momentum SC subband that has the strongest coupling to the semiconducting subband at low energies. The junction has length $L_J = 50$ nm and only consists of the semiconductor sites. For panels (a), (b), and (d), we use $d_L = 20$ nm, $a = 0.5$ nm, $\mu_{\rm sm} = 90$ meV, $\Delta_0 = 0.2$ meV, $t_c = 50$ meV, $t_{\rm sm} = \pm 2320$ meV, and $t_{\rm sc} = 144$ meV. In panel (a) $k_B T \approx 100$ mK. For panel (b) and for the light blue lines in panels (a) and (d), $\mu_{\rm sc} \approx 293$ meV (insulating phase), whereas for the dark blue lines in panels (a) and (d) $\mu_{\rm sc} \approx 306$ meV (superconducting phase). The currents are normalized to $I_0 = |e|\Delta_0 = 49$ nA. In panel (c), $N = 6000$, $\varphi = \pi$, while L_J, a, $\mu_{\rm sm}$ are the same as in panels (a), (b), and (d), and $\bar{\mu}_{\rm sc} = 5$ meV (18 meV) for the light blue (dark blue) wave functions.

strong coupling, while $E_g \sim \gamma(1 - \gamma/\Delta_0)$ for weak coupling, as already demonstrated in Ref. [47].

APPENDIX D: JOSEPHSON JUNCTION NUMERICS

The supercurrent through the JJ is calculated using kwant [72], following the methods described in Refs. [68–71]. The system consists of a junction region of length L_J, coupled to two semi-infinite leads. The Hamiltonian is treated in the framework of the tight-binding model. The semiconducting layer (one chain) extends over the entire setup. The junction consists only of semiconducting sites [shown in blue in Fig. 7(e)], whereas the leads consist of this semiconducting chain coupled to two SC strips of the finite width d_L, which implies that there are several occupied bands inside the leads, as can be seen in Fig. 7(b). In the regime of interest, there are several subbands with a positive effective mass (SC subbands) coupled to a single subband with a negative effective mass (semiconducting subband).

The Hamiltonian describing the junction is given by

$$H_J = \sum_{m=0}^{N_J-1} \psi_m^\dagger (2t_{\rm sm} - \mu_J)\eta_z \psi_m - \sum_{m=0}^{N_J-2} \psi_{m+1}^\dagger t_{\rm sm} \eta_z \psi_m + \text{H.c.}$$
$$= \boldsymbol{\psi}^\dagger \mathcal{H}_J \boldsymbol{\psi}, \tag{D1}$$

with $\psi_m^\dagger = (c_{m\uparrow}^\dagger, c_{m\downarrow})$, where $c_{m\uparrow}^\dagger$ creates a hole (electron) in the 1DHG (1DEG) at the mth site with spin $\uparrow$, and where N_J is the number of sites in the junction region. It should be noted that the sign of the chemical potential in the junction, μ_J, is adjusted in the 1DHG versus 1DEG calculation, to ensure that a positive chemical potential corresponds to

occupied subbands. Here, $t_{\rm sm} = 1/(2m_{\rm sm}a^2)$ describes the hopping inside the semiconductor, where $m_{\rm sm} \approx \pm 0.07 m_e$, and m_e is the free-electron mass and a denotes the lattice constant in the tight-binding chain. For convenience, we define $\boldsymbol{\psi}$ as the vector containing all ψ_m in the junction, which allows us to define the matrix representation of H_J, which we denote as $\mathcal{H}_J$.

As we consider finite-width leads, there are hopping matrix elements in both the longitudinal and transversal directions, and we work with the following Hamiltonians:

$$\begin{aligned} H_{{\rm lead},R} &= \sum_{\boldsymbol{n}=(N,0)}^{(\infty,\lfloor d_L/a\rfloor)} \psi_{\boldsymbol{n}}^\dagger h_{\boldsymbol{n}}^R \psi_{\boldsymbol{n}} \\ &\quad - \sum_{\boldsymbol{n}=(N,0)}^{(\infty,\lfloor d_L/a\rfloor)} \sum_{\boldsymbol{j}\in\{\hat{\boldsymbol{x}},\hat{\boldsymbol{z}}\}} \psi_{\boldsymbol{n}+\boldsymbol{j}}^\dagger T_{\boldsymbol{n}+\boldsymbol{j},\boldsymbol{n}} \psi_{\boldsymbol{n}} + \text{H.c.}, \\ H_{{\rm lead},L} &= \sum_{\boldsymbol{n}=(-1,0)}^{(-\infty,\lfloor d_L/a\rfloor)} \psi_{\boldsymbol{n}}^\dagger h_{\boldsymbol{n}}^L \psi_{\boldsymbol{n}} \\ &\quad - \sum_{\boldsymbol{n}=(-2,0)}^{(-\infty,\lfloor d_L/a\rfloor)} \sum_{\boldsymbol{j}\in\{\hat{\boldsymbol{x}},\hat{\boldsymbol{z}}\}} \psi_{\boldsymbol{n}+\boldsymbol{j}}^\dagger T_{\boldsymbol{n}+\boldsymbol{j},\boldsymbol{n}} \psi_{\boldsymbol{n}} + \text{H.c.}, \end{aligned} \tag{D2}$$

where $\boldsymbol{n} = (n_x, n_z)$ denotes the position of the site in the x and z directions as well as $\hat{\boldsymbol{x}}$ and $\hat{\boldsymbol{z}}$ are the unit vectors in the x and z directions, respectively. Here, $\psi_{(m,0)}^\dagger = \psi_m^\dagger$, where $\psi_m^\dagger$ is as defined above—this is a continuation of the semiconductor into the leads [see the blue sites in the leads in Fig. 7(e)]. On the other hand, for $n_z > 0$ the operator $\psi_{(n_x,n_z)}^\dagger = (d_{n_x,n_z,\uparrow}^\dagger, d_{n_x,n_z,\downarrow})$, where $d_{n_x,n_z,\sigma}^\dagger$ creates an electron with spin σ at site (n_x, n_z) in the superconducting strip. The onsite coefficients $h_{\boldsymbol{n}}^{L/R}$ and hopping coefficients $T_{\boldsymbol{m},\boldsymbol{n}}$ are defined as

$$h_{\boldsymbol{n}}^{L/R} = \begin{cases} (2t_{\rm sm} - \mu_{\rm sm})\eta_z, & \text{semiconducting site,} \\ (2t_{\rm sc} - \bar{\mu}_{\rm sc})\eta_z + \Delta_0\eta_x, & \text{SC site,} \end{cases} \tag{D3}$$

$$T_{\boldsymbol{m},\boldsymbol{n}} = \begin{cases} -t_{\rm sm}\eta_z, & \text{both sites are semiconducting,} \\ -t_{\rm sc}\eta_z, & \text{both sites are SC,} \\ -t_{\rm c}\eta_z, & \text{otherwise.} \end{cases} \tag{D4}$$

The hopping matrix element in the superconductor is given by $t_{\rm sc} = 1/(2m_{\rm sc}a^2)$, where $m_{\rm sc} \approx 0.95 m_e$ is the effective mass in the superconductor, while $\bar{\mu}_{\rm sc}$ sets the offset from half-filling of the lowest SC subband. The parameter $\mu_{\rm sm}$ is the effective chemical potential of the semiconducting subband, and hence sets the maximum (minimum) of the semiconducting hole-subband (electron-subband).

The leads are connected to the junction only through the semiconducting sites at the interface:

$$\begin{aligned} H_{J,{\rm lead}} &= -t_{\rm sm}[\psi_{(-1,0)}^\dagger \eta_z \psi_{(0,0)} + \psi_{(N-1,0)}^\dagger \eta_z e^{-i\eta_z\varphi/2} \psi_{(N,0)}] \\ &\quad + \text{H.c.}, \end{aligned} \tag{D5}$$

where the phase φ is the superconducting phase difference between the left and right superconductor. We have performed a gauge transformation in order to include φ as a hopping term between two sites at the interface between the junction and the leads. The gauge freedom allows us to place the complex phase $\exp(-i\eta_z\varphi/2)$ in the hopping between any two adjacent sites in the junction.

The SC strips are coupled to the semiconducting chain through an effective coupling $t_{\rm c}$. As $t_{\rm c} \lesssim \delta E_{\rm lead}, t_{\rm sm}, t_{\rm sc}$ (where $\delta E_{\rm lead}$ is the subband spacing in the lead), the majority of the contribution to the supercurrent comes from the coupling of the semiconducting subband to a single SC subband (for our parameters the SC subband that is closest to $E = 0$ and $k = 0$). This explains why increasing the chemical potential has little effect on the properties of the Josephson junction—this simply adds more weakly coupled bands at larger momenta but does not change the physics in the momentum and energy window that is of relevance to the Josephson junction.

To calculate the supercurrent through the junction, we use a Green's function approach, which is described in Refs. [68–71]. In this approach, we attach virtual leads at two adjacent sites (sites m and $m+1$) in the junction and calculate the following quantity:

$$\begin{aligned} I_{m,m+1}(\varphi) = |e|k_B T \sum_{n=0}^{\infty} \text{Im}\{\text{Tr}[\eta_z H_{m,m+1} G_{m+1,m}(i\omega_n, \varphi) \\ - \eta_z H_{m+1,m} G_{m,m+1}(i\omega_n, \varphi)]\}, \end{aligned} \tag{D6}$$

which describes the current between sites m and $m+1$. Here, e denotes the elementary charge, k_B is Boltzmann's constant, and T is the temperature of the system, which is taken to be significantly smaller than Δ_0/k_B. Here, $H_{m,m+1}$ is the matrix element of the tight-binding Hamiltonian that couples sites m and $m+1$ (hopping), while $G_{m,m+1}(i\omega_n, \varphi)$ is the Green's function matrix element that couples the same sites evaluated at the fermionic Matsubara frequency $i\omega_n$. The hopping matrix element is given by $H_{m,m+1} = t_{\rm sc}\eta_z$, while $G_{m+1,m}$ is calculated using the virtual leads and kwant [72].

The Nambu space Pauli matrix η_z in Eq. (D6) can be thought of as the BCS charge-matrix—the quasiparticles and quasiholes have opposite charges and will therefore have opposite contributions to the current. Since the system is a one-dimensional chain, calculating this for adjacent sites gives us the supercurrent through the entire junction. Furthermore, for our numerics, we truncate the Matsubara sum once the last term is smaller than 10^{-4} nA, such that the current has sufficiently converged. We take $k_B T = \Delta_0/20$, as this is the experimentally relevant temperature regime. This approach gives us the CPR, which we then use to calculate the critical supercurrent I_c (maximal value of the CPR) and the ratio of the first two harmonics of the CPR (see Fig. 3). As discussed in the main text, the ratio of the first two harmonics is a measure for the transparency of the junction.

We found that the CPRs obtained from this method are consistent with what is obtained from a finite system, where the current at phase difference φ is defined as $I(\varphi) = |e| \sum_{E(\varphi)<0} \frac{\partial E(\varphi)}{\partial \varphi}$, where $E(\varphi)$ are the negative eigenenergies of the finite system. However, using Eq. (D6) is computationally more efficient and allows us to consider infinite leads, which means that there are no finite-size effects.

1. Bound states in the Josephson junction

In the previous section, we gave a description of the numerical methods used to obtain the CPR through the junction. The critical current I_c is especially studied as a function of

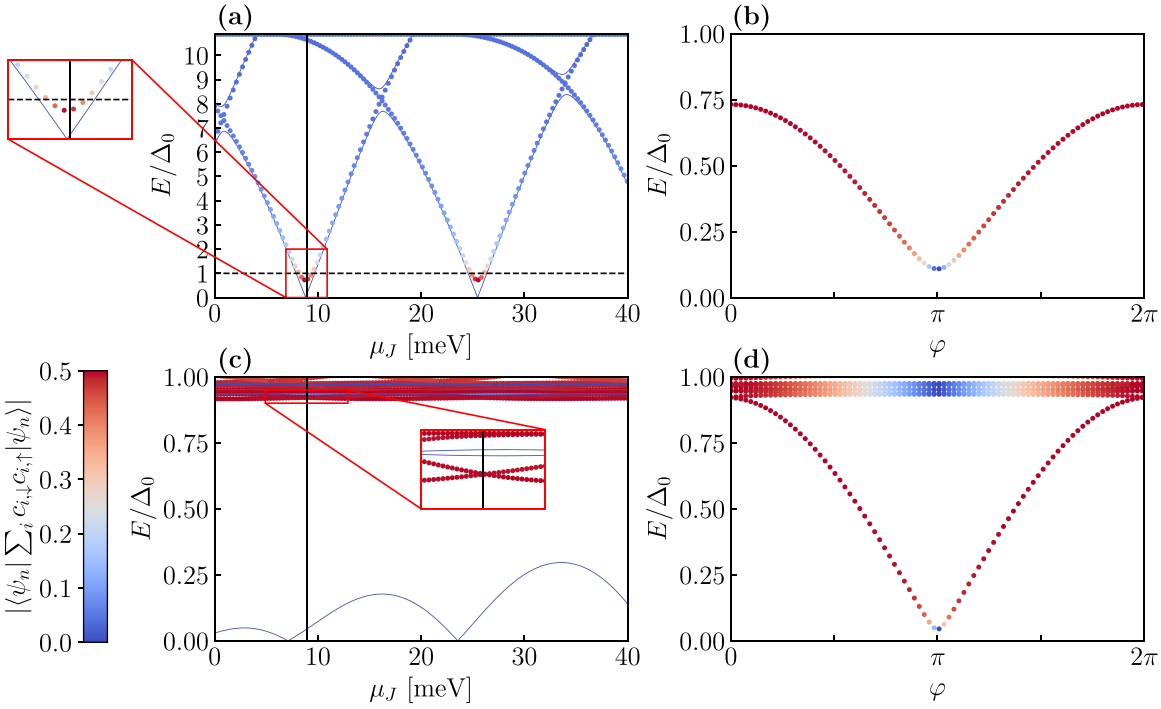

FIG. 8. Plots of bound state energies for a JJ vs chemical potential μ_J and superconducting phase φ for 1DHG [panels (a) and (b)] and 1DEG [panels (c) and (d)]. The bound states for a 1DHG are localized in the normal section of the JJ due to the insulating gaps in the leads and carry significant SC correlations only when their energies are below Δ_0 [which is indicated by the horizontal black dashed line in panel (a)]. (c) On the other hand, the ABSs that arise when the system is in the SC phase have a weaker dependence on μ_J, both in their energies and in the SC correlation. The dotted lines in panels (a) and (c) are for $\varphi = 0$, where the SC correlation is maximal, whereas the full lines (blue) are for $\varphi = \pi$, where the SC correlation is zero (in this case the pairing is Δ_0 in the left lead and $-\Delta_0$ in the right lead). In panel (b), we show the energy of the lowest bound state as function of φ for the leads being in the insulating phase at $\mu_J = 8.9$ meV [see vertical black line in panel (a)]. There are no states with energies just below the superconducting gap as well as there are no other states within the insulating gap, as can be seen in panel (a). For comparison, in panel (d), we show the energy-phase relation for the lowest $n = 12$ states for a 1DEG JJ with leads being in the SC proximity phase. Here, the ABS energy is around Δ_0 for φ close to zero and it almost merges with the bulk states. This is a reason why we included $\varphi = \pi$ in panel (c) to show the presence of the ABSs in the spectrum. The results are obtained from a finite-size system, with a single SC subband, described in Eqs. (D1) and (D2) with $d_L = 2a$. We used the following parameters: $L = 3500$ nm (total length of chain), $L_J = 62$ nm, $a = 1$ nm, $t_{\rm sm} = \pm 580$ meV, $t_{\rm sc} = 36.2$ meV, $t_c = 5$ meV, $\mu_{\rm sm} = 40$ meV, $\bar{\mu}_{\rm sc} = 2.5$ meV, and $\Delta_0 = 0.2$ meV. In panels (a) and (b), the effective masses have opposite signs, whereas in panels (c) and (d) they have the same signs.

μ_J, where it shows distinct peaks when the leads are in the insulating phase. These sharp peaks are attributed to bound states in the junction that are confined by the insulating gap in the leads. Thus, these bound states are present even without superconductivity (under the assumption that higher SC bands are only weakly coupled due to momentum mismatch), which can be seen from the normal state local density of states (LDOS) at zero energy [$\rho_n(0)$] in the junction shown in Fig. 7(d). We define $\rho_n(\omega)$ as

$$\rho_n(\omega) = \frac{2}{\pi}\mathrm{Im}\,\mathrm{tr}[G_n(\omega - i0^+)], \tag{D7}$$

where $G_n(\omega) = [\omega - \mathcal{H}_J - \Sigma_{\rm leads}(\omega)]^{-1}$ is the Green's function that describes the junction after integrating out the leads. The self-energy in the leads, $\Sigma_{\rm leads}(\omega)$, is obtained numerically using kwant [72].

The LDOS [see Fig. 7(d)] in the junction displays well-pronounced peaks at the same values of μ_J at which we observe peaks in I_c [see Fig. 7(a)] in the insulating phase. However, when the leads are in the SC phase, the μ_J dependence of I_c exhibits broad oscillations [which is the case when the 1DHG system is away from resonance or when the semiconductor is a 1DEG, see the dark blue curve in Fig. 7(a)]. These oscillations are due to Andreev bound states (ABS) weakly confined in the junction due to an SC gap in the leads. The energy separation between bound states, both in the insulating phase and in the SC phase, is defined by the length of the junction, which explains why the peaks in critical current have the same spacing in both phases (see Fig. 3). However, we note that the positions of the peaks in the I_c versus μ_J plot for 1DEG and 1DHG systems are generally not the same. Importantly, the ABS confined by the insulating gap in the leads have the similar pairing expectation values as the ABS confined by the proximity-induced pairing gap in the leads, provided that their energy does not deviated by more than Δ_0 from the chemical potential, which can be seen from Fig. 8.

We can gain further understanding of the peaks in I_c as a function of μ_J by considering a finite system, where we can explicitly calculate the wave functions. The wave function of a bound state (light blue), confined to the junction due the insulating gap in the leads, is much more localized compared

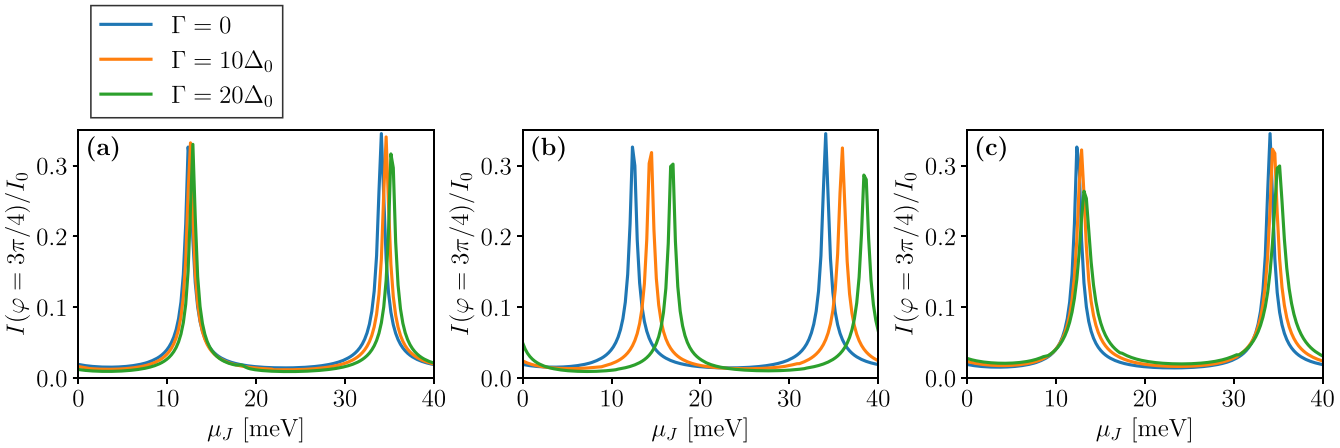

FIG. 9. In the insulating regime, the bound states in the junction give rise to sharp peaks in the supercurrent as a function of μ_J. However, the position and linewidth of these peaks could be affected by the disorder. In panels (a)–(c), we show the results for three typical disorder configurations. Generally, the height of peaks gets suppressed as disorder strength grows. (b) The peaks are often shifted compared to their positions in the absence of disorder. Interestingly, even in the strong disorder limit, $\Gamma = 20\Delta_0 = 4$ meV, the peaks in the supercurrent remain pronounced. The parameters are the same as in Fig. 8(a) and $N_{\max} = 300$.

to the wave function of an ABS (dark blue) confined by the proximity pairing gap, when the system is in the SC phase [see Fig. 7(c) where we plot the lowest-energy bound states, $|\psi_1\rangle$]. This is expected since the insulating gap is generally much larger than Δ_0 and thus the wave functions decay faster into the gapped region. In these finite-size system calculations, we consider only the lowest-momentum SC subband that is directly coupled to the semiconducting subband and neglect other superconducting subbands for simplicity.

While the sharp peaks in I_c are characteristic for the leads being in the insulating phase, they are still linked to the remaining superconducting pairing correlations of the strongly confined bound states with energies close to zero. Indeed, boundary effects at the junction interfaces, which mix-in locally also higher subbands of the superconductor, generate some SC correlations around the junction within coherence length $\xi_0 = v_F/\Delta_0$, whereas the leads far away from the junction (distances larger than ξ_0) are in the completely insulating phase without any SC correlations. In Fig. 8, we plot the energies of the bound states versus μ_J [Fig. 8(a)] in the insulating phase and [Fig. 8(c)] in the superconducting phase. Additionally, using the color scheme, we indicate the value of the SC correlation, $|\sum_i \langle\psi_n|c_{\uparrow,i}c_{\downarrow,i}|\psi_n\rangle|$, for the respective eigenstate $|\psi_n\rangle$ in the energy spectrum. As expected, the SC correlation is only significant in the insulating phase when $|E| < \Delta_0$ and when $\varphi = 0$. Interestingly, for $\varphi = \pi$, the SC correlation is zero in both [Fig. 8(a)] the insulating phase and [Fig. 8(c)] the superconducting phase. This is because the pairing is Δ_0 and $-\Delta_0$ in the left and right leads, respectively, which means that the sum over all sites in the system (the i sum above), will give contributions from the left side and the right side of the system, which cancel perfectly. The strong phase dependence of the bound state energy [shown in Fig. 8(b) for the insulating phase and Fig. 8(d) for the SC phase] confirms again that these are indeed bound states confined at the junction between two superconductors.

Throughout this work, we have considered Josephson junctions with highly transparent interfaces between the junction and the superconducting leads. This assumption is supported by experimental measurements demonstrating high transparency in similar setups [60]. However, it is important to point out that strong barriers at the junction ends could significantly impact our results. Such barriers can generate peaks in the supercurrent as a function of μ_J that resemble those we attribute to bound states formed by the insulating gap, even in the 1DEG system. Thus, it is important to emphasize that these sharp peaks in I_c versus μ_J, which are otherwise associated with a junction being in the weak transparency regime, can occur in the insulating phase in the leads. Thus, the insulating gap strongly suppresses the average junction transparency (the transparency is only of order unity, when μ_J is tuned to one of the peaks in I_c).

2. Robustness of I_c peaks in the presence of disorder

As discussed previously, disorder will inevitably be present in experimental setups. Therefore, it is important to investigate the effect of disorder on the peaks in I_c versus μ_J. In the finite system with a single SC subband [i.e., we set $d_L = 2a$ in Eq. (D2)], we introduce disorder to the onsite energies. The disorder is treated using a normal distribution, centered at zero with standard deviation Γ, which is added to the local chemical potentials ($\mu_{\rm sm}$ and $\mu_{\rm sc}$ for semiconducting and SC sites, respectively, and μ_J in the junction). The results are shown in Fig. 9, where we see that even for strong disorder, $\Gamma = 20\Delta_0$, the peaks in supercurrent are still present.

The current is calculated using [68,75]

$$I(\varphi) = |e| \sum_{n=1}^{N_{\max}} \frac{\partial E_n}{\partial \varphi}, \tag{D8}$$

where the summation should run over all occupied states (states with negative energy); however, states too far away from the chemical potential do not contribute, so we can cut the sum at some large value $N_{\max}$, chosen such that $I(\varphi)$ has already converged and does not depend on the choice of $N_{\max}$.

We assume that the energies are sorted such that $E_n > E_m$ for $m > n$, and that E_1 is the largest negative eigenvalue. The supercurrent is normalized relative to $I_0 = |e|\Delta_0 \approx 49\,\mathrm{nA}$, where e is the elementary charge. There could be slight shifts in the position of the peaks in the supercurrent because the disorder in the junction shifts energies of the bound states (see Fig. 9). The distance between peaks stays approximately the same. As expected, the results depend on the specific configuration of the disorder. However, from what we have observed, the peaks are present even for relatively strong disorder but their linewidth and shift in μ_J depend on the disorder strength and a given disorder configuration.

[1] G. Scappucci, C. Kloeffel, F. A. Zwanenburg, D. Loss, M. Myronov, J.-J. Zhang, S. De Franceschi, G. Katsaros, and M. Veldhorst, The germanium quantum information route, Nat. Rev. Mater. **6**, 926 (2020).

[2] R. Pillarisetty, Academic and industry research progress in germanium nanodevices, Nature (London) **479**, 324 (2011).

[3] G. Burkard, T. D. Ladd, A. Pan, J. M. Nichol, and J. R. Petta, Semiconductor spin qubits, Rev. Mod. Phys. **95**, 025003 (2023).

[4] C. Kloeffel, M. Trif, and D. Loss, Strong spin-orbit interaction and helical hole states in Ge/Si nanowire, Phys. Rev. B **84**, 195314 (2011).

[5] X.-J. Hao, T. Tu, G. Cao, C. Zhou, H.-O. Li, G.-C. Guo, W. Y. Fung, Z. Ji, G.-P. Guo, and W. Lu, Strong and tunable spin-orbit coupling of one-dimensional holes in Ge/Si core/shell nanowires, Nano Lett. **10**, 2956 (2010).

[6] Y. Hu, F. Kuemmeth, C. M. Lieber, and C. M. Marcus, Hole spin relaxation in Ge/Si core-shell nanowire qubits, Nat. Nanotechnol. **7**, 47 (2012).

[7] L. A. Terrazos, E. Marcellina, Z. Wang, S. N. Coppersmith, M. Friesen, A. R. Hamilton, X. Hu, B. Koiller, A. L. Saraiva, D. Culcer, and R. B. Capaz, Theory of hole-spin qubits in strained germanium quantum dots, Phys. Rev. B **103**, 125201 (2021).

[8] F. N. M. Froning, C. L. C., O. A. H. van der Molen, A. Li, E. P. A. M. Bakkers, D. M. Zumbühl, and F. R. Braakman, Ultrafast hole spin qubit with gate-tunable spin-orbit switch functionality, Nat. Nanotechnol. **16**, 308 (2021).

[9] H. Liu, T. Zhang, K. Wang, F. Gao, G. Xu, X. Zhang, S.-X. Li, G. Cao, T. Wang, J. Zhang, X. Hu, H.-O. Li, and G.-P. Guo, Gate-tunable spin-orbit coupling in a germanium hole double quantum dot, Phys. Rev. Appl. **17**, 044052 (2022).

[10] C. Adelsberger, M. Benito, S. Bosco, J. Klinovaja, and D. Loss, Hole-spin qubits in Ge nanowire quantum dots: Interplay of orbital magnetic field, strain, and growth direction, Phys. Rev. B **105**, 075308 (2022).

[11] D. V. Bulaev and D. Loss, Spin relaxation and decoherence of holes in quantum dots, Phys. Rev. Lett. **95**, 076805 (2005).

[12] S. Bosco, M. Benito, C. Adelsberger, and D. Loss, Squeezed hole spin qubits in Ge quantum dots with ultrafast gates at low power, Phys. Rev. B **104**, 115425 (2021).

[13] S. Bosco, B. Hetényi, and D. Loss, Hole spin qubits in Si FinFETs with fully tunable spin-orbit coupling and sweet spots for charge noise, PRX Quantum **2**, 010348 (2021).

[14] S. Bosco, P. Scarlino, J. Klinovaja, and D. Loss, Fully tunable longitudinal spin-photon interactions in Si and Ge quantum dots, Phys. Rev. Lett. **129**, 066801 (2022).

[15] M. J. Carballido, S. Svab, R. S. Eggli, T. Patlatiuk, P. Chevalier Kwon, J. Schuff, R. M. Kaiser, L. C. Camenzind, A. Li, N. Ares, E. P. A. M. Bakkers, S. Bosco, J. C. Egues, D. Loss, and D. M. Zumbühl, Compromise-free scaling of qubit speed and coherence, Nat. Commun. **16**, 7616 (2025).

[16] J. C. Abadillo-Uriel, E. A. Rodríguez-Mena, B. Martinez, and Y.-M. Niquet, Hole-spin driving by strain-induced spin-orbit interactions, Phys. Rev. Lett. **131**, 097002 (2023).

[17] N. W. Hendrickx, L. Massai, M. Mergenthaler, F. J. Schupp, S. Paredes, S. W. Bedell, G. Salis, and A. Fuhrer, Sweet-spot operation of a germanium hole spin qubit with highly anisotropic noise sensitivity, Nat. Mater. **23**, 920 (2024).

[18] C.-A. Wang, H. E. Ercan, M. F. Gyure, G. Scappucci, M. Veldhorst, and M. Rimbach-Russ, Modeling of planar germanium hole qubits in electric and magnetic fields, npj Quantum Inf. **10**, 102 (2024).

[19] S. Bosco and D. Loss, Fully tunable hyperfine interactions of hole spin qubits in Si and Ge quantum dots, Phys. Rev. Lett. **127**, 190501 (2021).

[20] Y. Hu, H. O. H. Churchill, D. J. Reilly, J. Xiang, C. M. Lieber, and C. M. Marcus, A Ge/Si heterostructure nanowire-based double quantum dot with integrated charge sensor, Nat. Nanotechnol. **2**, 622 (2007).

[21] J. Fischer, W. A. Coish, D. V. Bulaev, and D. Loss, Spin decoherence of a heavy hole coupled to nuclear spins in a quantum dot, Phys. Rev. B **78**, 155329 (2008).

[22] L. C. Camenzind, S. Geyer, A. Fuhrer, R. J. Warburton, D. M. Zumbühl, and A. V. Kuhlmann, A hole spin qubit in a fin field-effect transistor above 4 kelvin, Nat. Electron. **5**, 178 (2022).

[23] S. Geyer, B. Hetényi, S. Bosco, L. C. Camenzind, R. S. Eggli, A. Fuhrer, D. Loss, R. J. Warburton, D. M. Zumbühl, and A. V. Kuhlmann, Anisotropic exchange interaction of two hole-spin qubits, Nat. Phys. **20**, 1152 (2024).

[24] S. D. Liles, D. J. Halverson, Z. Wang, A. Shamim, R. S. Eggli, I. K. Jin, J. Hillier, K. Kumar, I. Vorreiter, M. J. Rendell, J. Y. Huang, C. C. Escott, F. E. Hudson, W. H. Lim, D. Culcer, A. S. Dzurak, and A. R. Hamilton, A singlet-triplet hole-spin qubit in MOS silicon, Nat. Commun. **15**, 7690 (2024).

[25] C.-A. Wang, V. John, H. Tidjani, C. X. Yu, A. S. Ivlev, C. Déprez, F. van Riggelen-Doelman, B. D. Woods, N. W. Hendrickx, W. I. L. Lawrie, L. E. A. Stehouwer, S. D. Oosterhout, A. Sammak, M. Friesen, G. Scappucci, S. L. de Snoo, M. Rimbach-Russ, F. Borsoi, and M. Veldhorst, Operating semiconductor quantum processors with hopping spins, Science **385**, 447 (2024).

[26] F. Borsoi, N. W. Hendrickx, V. John, M. Meyer, S. Motz, F. van Riggelen, A. Sammak, S. L. de Snoo, G. Scappucci, and M. Veldhorst, Shared control of a 16 semiconductor quantum dot crossbar array, Nat. Nanotechnol. **19**, 21 (2024).

[27] X. Zhang, E. Morozova, M. Rimbach-Russ, D. Jirovec, T.-K. Hsiao, P. C. Fariña, C.-A. Wang, S. D. Oosterhout, A. Sammak, G. Scappucci, M. Veldhorst, and L. M. K. Vandersypen, Universal control of four singlet–triplet qubits, Nat. Nanotechnol. **20**, 209 (2024).

[28] D. Jirovec, A. Hofmann, A. Ballabio, P. M. Mutter, G. Tavani, M. Botifoll, A. Crippa, J. Kukucka, O. Sagi, F. Martins, J.

Saez-Mollejo, I. Prieto, M. Borovkov, J. Arbiol, D. Chrastina, G. Isella, and G. Katsaros, A singlet-triplet hole spin qubit in planar Ge, Nat. Mater. **20**, 1106 (2021).

[29] J. Saez-Mollejo, D. Jirovec, Y. Schell, J. Kukucka, S. Calcaterra, D. Chrastina, G. Isella, M. Rimbach-Russ, S. Bosco, and G. Katsaros, Exchange anisotropies in microwave-driven singlet-triplet qubits, Nat. Commun. **16**, 3862 (2025).

[30] J. Xiang, A. Vidan, M. Tinkham, R. M. Westervelt, and C. M. Lieber, Ge/Si nanowire mesoscopic Josephson junctions, Nat. Nanotechnol. **1**, 208 (2006).

[31] M. Valentini, O. Sagi, L. Baghumyan, T. de Gijsel, J. Jung, S. Calcaterra, A. Ballabio, J. Aguilera Servin, K. Aggarwal, M. Janik, T. Adletzberger, R. Seoane Souto, M. Leijnse, J. Danon, C. Schrade, E. Bakkers, D. Chrastina, G. Isella, and G. Katsaros, Parity-conserving Cooper-pair transport and ideal superconducting diode in planar germanium, Nat. Commun. **15**, 169 (2024).

[32] M. Valentini, Mesoscopic phenomena in hybrid semiconductor-superconductor nanodevices: From full-shell nanowires to two-dimensional hole gas in germanium, Ph.D. dissertation, Institute of Science and Technology Austria, 2023.

[33] W. Chang, S. Albrecht, T. Jespersen, F. Kuemmeth, P. Krogstrup, J. Nygård, and C. M. Marcus, Hard gap in epitaxial semiconductor–superconductor nanowires, Nat. Nanotechnol. **10**, 232 (2015).

[34] E. J. H. Lee, X. Jiang, M. Houzet, R. Aguado, C. M. Lieber, and S. De Franceschi, Spin-resolved Andreev levels and parity crossings in hybrid superconductor–semiconductor nanostructures, Nat. Nanotechnol. **9**, 79 (2014).

[35] S. Park and A. L. Yeyati, Andreev spin qubits in multichannel Rashba nanowires, Phys. Rev. B **96**, 125416 (2017).

[36] M. Hays, V. Fatemi, D. Bouman, J. Cerrillo, S. Diamond, K. Serniak, T. Connolly, P. Krogstrup, J. Nygård, A. L. Yeyati, A. Geresdi, and M. H. Devoret, Coherent manipulation of an Andreev spin qubit, Science **373**, 430 (2021).

[37] M. Spethmann, X.-P. Zhang, J. Klinovaja, and D. Loss, Coupled superconducting spin qubits with spin-orbit interaction, Phys. Rev. B **106**, 115411 (2022).

[38] A. Y. Kitaev, Unpaired Majorana fermions in quantum wires, Phys.-Usp. **44**, 131 (2001).

[39] M. Luethi, K. Laubscher, S. Bosco, D. Loss, and J. Klinovaja, Planar Josephson junctions in germanium: Effect of cubic spin-orbit interaction, Phys. Rev. B **107**, 035435 (2023).

[40] M. Luethi, H. F. Legg, K. Laubscher, D. Loss, and J. Klinovaja, Majorana bound states in germanium Josephson junctions via phase control, Phys. Rev. B **108**, 195406 (2023).

[41] C. Nayak, S. H. Simon, A. Stern, M. Freedman, and S. Das Sarma, Non-Abelian anyons and topological quantum computation, Rev. Mod. Phys. **80**, 1083 (2008).

[42] F. Maier, J. Klinovaja, and D. Loss, Majorana fermions in Ge/Si hole nanowires, Phys. Rev. B **90**, 195421 (2014).

[43] K. Laubscher, J. D. Sau, and S. Das Sarma, Majorana zero modes in gate-defined germanium hole nanowires, Phys. Rev. B **109**, 035433 (2024).

[44] C. Reeg, D. Loss, and J. Klinovaja, Finite-size effects in a nanowire strongly coupled to a thin superconducting shell, Phys. Rev. B **96**, 125426 (2017).

[45] C. Reeg, D. Loss, and J. Klinovaja, Proximity effect in a two-dimensional electron gas coupled to a thin superconducting layer, Beilstein J. Nanotechnol. **9**, 1263 (2018).

[46] C. Reeg, D. Loss, and J. Klinovaja, Metallization of a Rashba wire by a superconducting layer in the strong-proximity regime, Phys. Rev. B **97**, 165425 (2018).

[47] N. B. Kopnin and A. S. Melnikov, Proximity-induced superconductivity in two-dimensional electronic systems, Phys. Rev. B **84**, 064524 (2011).

[48] N. van Loo, G. P. Mazur, T. Dvir, G. Wang, R. C. Dekker, J.-Y. Wang, M. Lemang, C. Sfiligoj, A. Bordin, D. van Driel, G. Badawy, S. Gazibegovic, E. P. A. M. Bakkers, and L. P. Kouwenhoven, Electrostatic control of the proximity effect in the bulk of semiconductor-superconductor hybrids, Nat. Commun. **14**, 3325 (2023).

[49] M. Sütő, T. A. Prok, P. Makk, M. Kirti, G. Biasiol, S. Csonka, and E. Tóvári, Near-surface InAs two-dimensional electron gas on a GaAs substrate: Characterization and superconducting proximity effect, Phys. Rev. B **106**, 235404 (2022).

[50] W. Mayer, J. Yuan, K. S. Wickramasinghe, T. Nguyen, M. C. Dartiailh, and J. Shabani, Superconducting proximity effect in epitaxial Al-InAs heterostructures, Appl. Phys. Lett. **114**, 103104 (2019).

[51] H. Takayanagi and T. Kawakami, Superconducting proximity effect in the native inversion layer on InAs, Phys. Rev. Lett. **54**, 2449 (1985).

[52] C. Adelsberger, H. F. Legg, D. Loss, and J. Klinovaja, Microscopic analysis of proximity-induced superconductivity and metallization effects in superconductor-germanium hole nanowires, Phys. Rev. B **108**, 155433 (2023).

[53] T. D. Stanescu and S. Das Sarma, Proximity-induced superconductivity generated by thin films: Effects of Fermi surface mismatch and disorder in the superconductor, Phys. Rev. B **106**, 085429 (2022).

[54] N. W. Hendrickx, D. P. Franke, A. Sammak, M. Kouwenhoven, D. Sabbagh, L. Yeoh, R. Li, M. L. V. Tagliaferri, M. Virgilio, G. Capellini, G. Scappucci, and M. Veldhorst, Gate-controlled quantum dots and superconductivity in planar germanium, Nat. Commun. **9**, 2835 (2018).

[55] J. Ridderbos, M. Brauns, J. Shen, F. K. de Vries, A. Li, E. P. A. M. Bakkers, A. Brinkman, and F. A. Zwanenburg, Josephson effect in a few-hole quantum dot, Adv. Mater. **30**, 1802257 (2018).

[56] N. W. Hendrickx, M. L. V. Tagliaferri, M. Kouwenhoven, R. Li, D. P. Franke, A. Sammak, A. Brinkman, G. Scappucci, and M. Veldhorst, Ballistic supercurrent discretization and micrometer-long Josephson coupling in germanium, Phys. Rev. B **99**, 075435 (2019).

[57] F. Vigneau, R. Mizokuchi, D. C. Zanuz, X. Huang, S. Tan, R. Maurand, S. Frolov, A. Sammak, G. Scappucci, F. Lefloch, and S. De Franceschi, Germanium quantum-well Josephson field-effect transistors and interferometers, Nano Lett. **19**, 1023 (2019).

[58] J. Ridderbos, M. Brauns, F. K. de Vries, J. Shen, A. Li, S. Kölling, M. A. Verheijen, A. Brinkman, W. G. van der Wiel, E. P. A. M. Bakkers, and F. A. Zwanenburg, Hard superconducting gap and diffusion-induced superconductors in Ge-Si nanowires, Nano Lett. **20**, 122 (2020).

[59] K. Aggarwal, A. Hofmann, D. Jirovec, I. Prieto, A. Sammak, M. Botifoll, S. Martí-Sánchez, M. Veldhorst, J. Arbiol, G. Scappucci, J. Danon, and G. Katsaros, Enhancement of

proximity-induced superconductivity in a planar Ge hole gas, Phys. Rev. Res. **3**, L022005 (2021).

[60] A. Tosato, *et al.*, Hard superconducting gap in germanium, Commun. Mater. **4**, 23 (2023).

[61] E. Zhuo, Z. Lyu, X. Sun, A. Li, B. Li, Z. Ji, J. Fan, E. Bakkers, X. Han, X. Song, F. Qu, G. Liu, J. Shen, and L. Lu, Hole-type superconducting gatemon qubit based on Ge/Si core/shell nanowires, npj Quantum Inf. **9**, 51 (2023).

[62] A. G. Moghaddam, T. Kernreiter, M. Governale, and U. Zülicke, Exporting superconductivity across the gap: Proximity effect for semiconductor valence-band states due to contact with a simple-metal superconductor, Phys. Rev. B **89**, 184507 (2014).

[63] S. S. Babkin, B. Joecker, K. Flensberg, M. Serbyn, and J. Danon, Superconducting proximity effect in two-dimensional hole gases, Phys. Rev. B **111**, 214518 (2025).

[64] D. M. Pino, R. S. Souto, M. J. Calderón, R. Aguado, and J. C. Abadillo-Uriel, Theory of superconducting proximity effect in hole-based hybrid semiconductor-superconductor devices, Phys. Rev. B **111**, 235443 (2025).

[65] J. A. Steele, P. J. Strohbeen, C. Verdi, A. Baktash, A. Danilenko, Y.-H. Chen, J. van Dijk, L. Wang, E. Demler, S. Salmani-Rezaie, P. Jacobson, and J. Shabani, Superconductivity in substitutional Ga-hyperdoped Ge epitaxial thin films, Nat. Nanotechnol. **20**, 1757 (2025).

[66] L. Lakic, W. I. L. Lawrie, D. van Driel, L. E. A. Stehouwer, Y. Su, M. Veldhorst, G. Scappucci, F. Kuemmeth, and A. Chatterjee, A quantum dot in germanium proximitized by a superconductor, Nat. Mater. **24**, 552 (2025).

[67] E. Marcellina, A. R. Hamilton, R. Winkler, and D. Culcer, Spin-orbit interactions in inversion-asymmetric two-dimensional hole systems: A variational analysis, Phys. Rev. B **95**, 075305 (2017).

[68] R. Hess, H. F. Legg, D. Loss, and J. Klinovaja, Josephson transistor from the superconducting diode effect in domain wall and skyrmion magnetic racetracks, Phys. Rev. B **108**, 174516 (2023).

[69] A. Levy Yeyati, A. Martín-Rodero, and F. J. García-Vidal, Self-consistent theory of superconducting mesoscopic weak links, Phys. Rev. B **51**, 3743 (1995).

[70] F. K. de Vries, T. Timmerman, V. P. Ostroukh, J. van Veen, A. J. A. Beukman, F. Qu, M. Wimmer, B.-M. Nguyen, A. A. Kiselev, W. Yi, M. Sokolich, M. J. Manfra, C. M. Marcus, and L. P. Kouwenhoven, h/e superconducting quantum interference through trivial edge states in InAs, Phys. Rev. Lett. **120**, 047702 (2018).

[71] W. Himmler, R. Fischer, M. Barth, J. Fuchs, D. A. Kozlov, N. N. Mikhailov, S. A. Dvoretsky, C. Strunk, C. Gorini, K. Richter, and D. Weiss, Supercurrent interference in HgTe-wire Josephson junctions, Phys. Rev. Res. **5**, 043021 (2023).

[72] C. W. Groth, M. Wimmer, A. R. Akhmerov, and X. Waintal, kwant: A software package for quantum transport, New J. Phys. **16**, 063065 (2014).

[73] C. Ciaccia, R. Haller, A. Drachmann, T. Lindemann, M. Manfra, C. Schrade, and C. Schoenenberger, Charge-4e supercurrent in a two-dimensional InAs-Al superconductor-semiconductor heterostructure, Commun. Phys. **7**, 41 (2024).

[74] D. Willsch, *et al.*, Observation of Josephson harmonics in tunnel junctions, Nat. Phys. **20**, 815 (2024).

[75] H. F. Legg, K. Laubscher, D. Loss, and J. Klinovaja, Parity-protected superconducting diode effect in topological Josephson junctions, Phys. Rev. B **108**, 214520 (2023).

[76] P. D. Johannsen, H. Legg, S. Bosco, D. Loss, and J. Klinovaja, Data and code for "Atypical Josephson effect in hybrid superconductor-hole systems", Zenodo (2026), https://doi.org/10.5281/zenodo.18409848.